Doctoral Thesis in Physics

The tunnel magneto-Seebeck effect in magnetic tunnel junctions with $MgAl_2O_4$ barrier

Paving the way towards spin caloritronic applications

Torsten Hübner

Bielefeld University, Department of Physics

September 2017

Declaration of academic honesty

I hereby declare that the doctoral thesis at hand is entirely my own work and that no part of it has been written or provided by another person and that no part of it has been copied from another person's work or any other source. Additionally, I declare that all referenced work from other people is cited correctly and that it can be found in the bibliography.

Bielefeld, September 4, 2017

(Torsten Hübner)

Reviewers:
Prof. Dr. Günter Reiss, Bielefeld University
Prof. Dr. Thomas Huser, Bielefeld University

Printed on non-aging paper ISO 9706
Bielefeld University, Department of Physics
Center for Spinelectronic Materials and Devices

Man muß nichts im Leben fürchten, man muß nur alles verstehen.

Marie Skłodowska Curie

Kurzfassung

Das Thema der vorliegenden Doktorarbeit ist der Tunnel Magneto-Seebeck (TMS) Effekt, der ein Paradebeispiel für das erst entstehende Wissenschaftsfeld der Spinkaloritronik ist. Die Spinkaloritronik beschäftigt sich mit dem Zusammenspiel von Ladungs-, Thermo- und Spinströmen, wobei das Ziel die Entwicklung neuer Datenspeicher oder die Verbesserung bestehender Technologien ist. Insbesondere steht dabei die nicht nutzbare Abwärme heutiger technischer Anwendungen im Fokus. Mit dem TMS Effekt ist es möglich eine Temperaturdifferenz, die sich über wenige Nanometer erstreckt, mittels Spinströmen in eine messbare Spannung umzuwandeln. Dafür werden magnetische Tunnelelemente genutzt, die die Basis vieler Forschungsfelder und Anwendungen bilden. In dieser Arbeit wird $MgAl_2O_4$ (MAO) als Tunnelbarriere im Vergleich zum häufig verwendeten MgO untersucht. Mittlerweile gibt es mehrere etablierte Methoden, um experimentell eine Temperaturdifferenz in Tunnelelementen zu erzeugen und damit den TMS Effekt zu untersuchen.

Innerhalb dieser Arbeit wird das laserinduzierte Heizen genutzt, um die Ergebnisse mit einem intrinsischen TMS Effekt zu vergleichen, der durch eine mathematische Symmetrieanalyse der experimentellen Ergebnisse ermittelt wird. Die wichtigsten Ergebnisse dieser Untersuchungen sind die Untauglichkeit der Symmetrieanalyse im Hinblick auf die Identifizierung eines intrinsischen TMS Effekts und die materialunabhängige Verdopplung der Schaltamplitude bei dicken Barrieren. Durch seine geringe thermische Leitfähigkeit stellt sich MAO als geeigneter Kandidat für die Generierung von Thermospannungen heraus. Außerdem gewähren Simulationen der Temperaturverteilungen neue Einblicke in die thermische Leitfähigkeit einer dünnen isolierenden Schicht.

Insgesamt trägt diese Arbeit zu einem grundlegenden Verständnis von thermisch induzierten und Spinstrom-basierten Effekten in Nanostrukturen bei und ebnet damit den Weg für zukünftige technische Anwendungen.

Abstract

The topic of the doctoral thesis at hand is the tunnel magneto-Seebeck (TMS) effect, which is a textbook example of the emerging research field of spin caloritronics. Spin caloritronics deals with the interplay of charge, heat and spin currents with the goal of developing new data storage techniques or the improvement of existing technologies. In particular, it focuses on the waste heat of today's devices. With the TMS effect it is possible to convert a temperature difference, which extends over several nanometers only, to a measurable voltage based on spin currents. For this, magnetic tunnel junctions are used, which are the foundation of many research areas and applications. In this work, $MgAl_2O_4$ (MAO) is investigated as tunnel barrier in comparison to the frequently used MgO. By now, several methods are available to create a temperature difference in tunnel junctions to study the tunnel magneto-Seebeck effect.

Within this work, the laser-induced heating is used in order to compare its results with an intrinsic TMS effect, which is determined by a mathematical symmetry analysis of the experimental results. The most important results of these investigations are the unsuitability of the symmetry analysis with regard to the identification of an intrinsic TMS effect and the material-independent doubling of the switching ratio in case of thick barriers. Due to its low thermal conductivity, MAO presents itself as suitable candidate for the generation of thermovoltages. Furthermore, simulations of the temperature distributions offer new insights into the thermal conductivity of a thin insulating film.

Overall, this work contributes to a fundamental understanding of thermally induced and spin-current based effects in nanostructures and paves the way towards future technical applications.

Contents

1. Motivation

For decades, the famous prediction of Gordon Moore, called Moore's law [1], about the log-linear connection between time and circuit density propelled the semiconductor industry. It forms the basis of the International Technology Roadmap for Semiconductors (ITRS) [2], which predicts the desired future technology nodes for the industry. Thus, since 1971, this concept can be considered a successful self-fulfilling prophecy.

Figure 1.1(a) shows the size evolution of computational devices over time. A new machine is introduced to the market about every ten years. At the same time, Fig. 1.1(b) presents the development of the transistor density and the clock speeds of the corresponding devices. Nowadays, the semiconductor industry has almost reached the natural limit of feature sizes, which is for example visible in the saturation of the clock speeds in

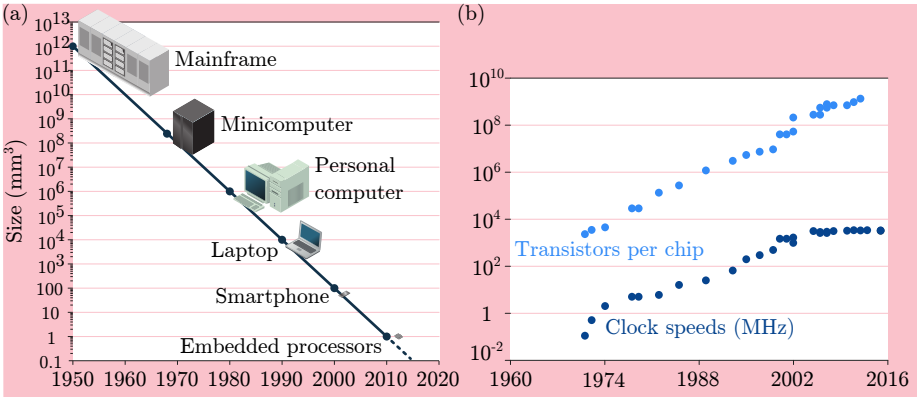

Figure 1.1.: (a) Size evolution of computational devices. About every ten years, a new machine is developed. (b) Transistors per chip (light blue) and corresponding clock speeds (dark blue) from 1960 to 2016. Pictures taken from Ref. [3].

the early 2000s. Here, the continued shrinking resulted in uncontrollable heating of the chips, effectively setting an upper limit to the clock speeds. However, Moore's law was kept alive by using multiple (two, four, eight) processors on each chip. Nevertheless, with the 5 nm node coming in $\approx$ 2020, the scaling-down and, hence, Moore's law is believed to come to an end [3]. Therefore, new paths of data storage, processing and handling are inevitable.

Many technical applications of today function on the basis of spintronic effects such as the tunnel magnetoresistance (TMR). After years of improving effect sizes and optimizing material parameters, reaching a TMR effect of over 600 % at room temperature [4], devices based on the TMR effect, for example a magnetic tunnel junction (MTJ), became indispensable for both industry and research. Exemplary applications range from magnet, current, angle and position sensors to bank note validators and magnetic ink readers [5].

In addition to the spin-polarized currents exploited in MTJs, heat currents gained more and more attraction in recent years. Reference [6] shows a flow chart of the different energy resources and their usage within the USA. Here, two thirds of the overall energy are labeled as rejected energy or, in other terms, waste heat. One new path might be offered by the controlled utilization of the otherwise wasted heat in today's devices. A directed use of thermal flows in nano-sized structures could potentially overcome the aforementioned problems of such devices. The combination of heat, charge and spin currents is realized within the emerging research field of spin caloritronics, which was started by Johnson and Silsbee [7] with the discovery of heat currents also interacting with spin currents. After the first report of an experimental conversion of a heat current into a measurable voltage via the spin Seebeck effect [8], the term 'spin caloritronics' was coined by Bauer et al. [9], who also published a detailed review [10].

One of the key effects within the field of spin caloritronics is the tunnel magneto-Seebeck (TMS) effect, which describes the response of an MTJ that is subject to a temperature gradient. The resulting temperature difference generates a thermovoltage without any external bias voltage across the MTJ. Similar to the TMR, this thermovoltage depends on

the magnetic state of the MTJ. First theoretical predictions were done by Czerner et al. [11], while experimental proof was provided shortly after by Walter et al. [12] and Liebing et al. [13]. This effect might boost spin caloritronic applications as did the TMR effect with spintronic applications. Accordingly, the goal is to develop devices that are more efficient and pave the way towards less energy-consuming technologies. A major advantage of this approach is the usage of MTJs, which are well known and established systems. However, up to now, the TMS has mostly been studied at CoFeB/MgO/CoFeB MTJs with a standard MgO barrier thickness of around 2.0 nm.

Thus, in the work at hand the TMS effect and the resulting thermovoltage are studied for MTJs with different barrier materials and barrier thicknesses in order to find optimized parameters for future applications. Furthermore, the aim of this work is to establish a profound understanding of the thermal distributions and the accompanied effects within nano-sized structures such as MTJs. For this analysis, finite element simulations are used to interpret the results.

This work is organized as follows: The first part provides a profound theoretical basis of MTJs, the TMR and the TMS effect. In the second part, the used materials and methods are presented in detail. Part three is comprised of both the results and the corresponding discussion of the measurements. Lastly, the fourth part summarizes the results of this work and offers an outlook on further ideas regarding the tunnel magneto-Seebeck effect and future technical applications.

Part I.

Theory

2. Magnetic tunnel junctions

On the following pages, the concept of MTJs is described in more detail. This concept is based on the tunneling of electrons with kinetic energy E_k through a barrier of potential energy φ and thickness d. In case of classical mechanics, the transmission T of the electron is 0 and the reflectivity R is 1, if $E_\mathrm{k} < \varphi$ and vice versa. However, the wave character of the electron results in a non-zero transmission probability across the barrier even if $E_\mathrm{k} < \varphi$, which is why the origin of tunneling is purely based on quantum mechanics [14].

In addition to the barrier, MTJs consist of two ferromagnetic electrodes on either side of the barrier. Accordingly, the tunnel current across the barrier depends on the band structure of both ferromagnets, which, in turn, depends on the relative magnetization alignment, which can be, with no loss of generality, either parallel (p) or antiparallel (ap). The first measurements of Fe/Ge/Co MTJs revealed a conductance change of 14 % at low temperatures when changing from parallel to antiparallel alignment of the two ferromagnetic electrodes [15]. In his work, Julliere assumed the spin of the electrons to be conserved during tunneling and, thus, developed a two-current model to explain his observations.

Based on this assumption, Slonczewski [16] found the spin dependent transmission $T_{\uparrow,\downarrow}$ to be proportional to $\exp\left(-k_{\uparrow,\downarrow}\varphi^{\frac{1}{2}}d\right)$, with the complex wave vector of the electrons $k_{\uparrow,\downarrow}$ for spin up ($\uparrow$) and spin down ($\downarrow$). Moodera et al. and Miyazaki et al. [17, 18] studied $Co/Al_2O_3/NiFe$ and $Fe/Al_2O_3/Fe$ MTJs at room temperature and found a relative resistance change between the p and ap magnetization alignment of the electrodes of around 15 %. This resistance change is called the TMR effect and is discussed in the following sections.

2.1. The tunnel magnetoresistance effect

In general, the TMR effect is defined as the relative resistance change measured between the parallel (R_p) and antiparallel (R_ap) state that can be expressed (in the two-current model) by the spin polarizations $P_{1,2}$ of the two ferromagnetic electrodes such that

$$\mathrm{TMR} = \frac{R_\mathrm{ap} - R_\mathrm{p}}{R_\mathrm{p}} = \frac{2P_1P_2}{1 - P_1P_2}. \tag{2.1}$$

For the experimental determination of the TMR, a small bias voltage is applied to the MTJ to define the direction of the tunneling current and an external magnetic field is used to change the magnetization alignment of the ferromagnetic electrodes. Usually, the magnetization of the thin ferromagnetic electrodes is orientated in the plane of the stack due to shape anisotropy and, thus, the magnetic field is applied in the plane of the stack as well. A schematic representation of the TMR effect is depicted in Fig. 2.1. In order to observe the TMR effect, different switching fields of the electrodes are needed in first place. Usually, this difference is achieved by either using a hard and a soft magnetic electrode (e.g. by different thicknesses, see Fig. 2.1(a)) or by utilizing the exchange bias effect [19] of an antiferromagnet close to one of the ferromagnets (see Fig. 2.1(b)).

In addition to the major loops shown in Figs. 2.1(a,b), where both the soft and the hard magnetic electrode change their magnetic state, a minor loop (Fig. 2.1(c)) describes the switching of only one electrode, namely the soft magnetic one.

The resistance change between p and ap state can be understood within the free electron model, which is also called the Drude-Sommerfeld model [20]. Here, the density of states (DOS) is proportional to the square root of the electron energy, i.e., DOS $\propto \sqrt{\mathrm{E}}$. The resulting tunnel currents that lead to the TMR effect are spin dependently summed up in Fig. 2.2.

Again, spin flip transitions are excluded. In the antiparallel state (see Fig. 2.2(a)), either more initial than final states or more final than initial states are available. In contrast, a large current is expected in the parallel

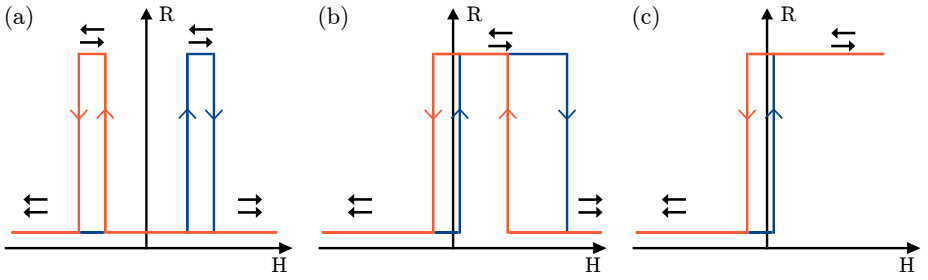

Figure 2.1.: (a) Ideal major loop of an MTJ with one soft and one hard magnetic electrode, and (b) with an additional exchange bias. (c) Ideal minor loop of an exchange biased MTJ. The black arrows indicate the parallel and antiparallel magnetization alignment, respectively. The colored arrows indicate the direction of the external magnetic field H. R is the corresponding resistance.

state due to the large amount of initial and final states for the majority electrons (see Fig. 2.2(b)). This difference in tunneling currents gives rise to a lower resistance in the parallel state than in the antiparallel state and, thus, to the TMR effect.

Since the electronic structure of the barrier is not taken into account in the preceding discussion, but plays a vital role when dealing with very high TMR ratios of several hundred %, the next section deals with the effect of coherent tunneling.

2.2. Coherent tunneling

The two-current model and the resulting TMR effect introduced by Julliere is considered to be fully incoherent, since no assumptions about the electronic structure of the barrier are made. Thus, all states have the same tunneling probability. Experiments with amorphous Al-O barriers agree very well with the theoretical predictions of Julliere's model [21,22], although, it was found that the tunneling probabilities of the involved states in fact depend on their symmetry [23, 24]. If the symmetry of the state is conserved during the tunneling process, the tunneling is called

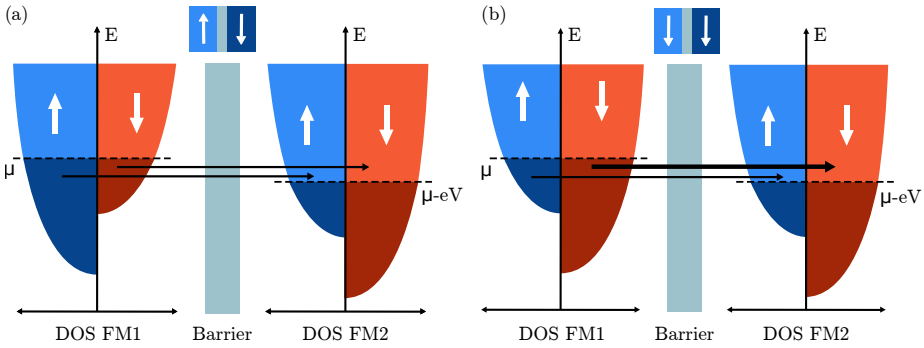

Figure 2.2.: (a) Tunnel currents in the antiparallel and (b) parallel state with an applied bias voltage eV. The large amount of initial and final states for the majority electrons in the parallel state causes a large tunnel current in comparison to the antiparallel state, highlighted by the thickness of the arrows.

coherent.

In typical electrodes like Co or Fe, the states with Δ_1 symmetry exhibit full spin polarization ($P = 1$) at the Fermi energy. Thus, very large TMR ratios are expected if only Δ_1 (s-like character) states contribute to the tunneling current. However, in case of Al-O barriers, states with Δ_2 and Δ_5 (d-like character, $P > 0$) add a considerable contribution to the overall current, effectively reducing the spin polarization and the TMR ratio.

Figures 2.3(a,b) display the states and their corresponding symmetries that take part in the tunneling process. While in case of an amorphous Al-O barrier all states contribute equally, this is not the case for a crystalline MgO barrier. Here, the tunneling current is almost entirely carried by Δ_1 states.

This difference is attributed to the different decay lengths of the states within the MgO barrier in contrast to the Al-O barrier (cf. Fig. 2.3(c)). Δ_1 states in an epitaxial Fe/MgO/Fe MTJ exhibit a decay time that is orders below the decay time of $\Delta_{2,5}$ states. Thus, the tunneling current is dominated by the fully spin polarized Δ_1 states, which results in very high TMR ratios. This effect is called the Δ_1 symmetry filter effect and

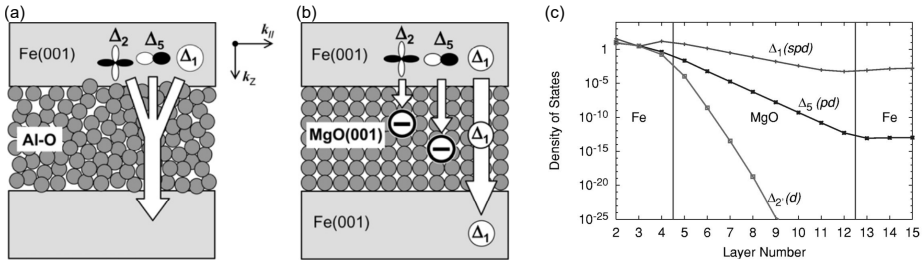

Figure 2.3.: (a,b) Tunneling process of states with different symmetries through an amorphous Al-O and a crystalline MgO barrier, respectively. (c) Decay times of the evanescent states in an MgO barrier sandwiched by two Fe electrodes in the parallel state. Adopted from Refs. [25, 26].

is at present exploited in CoFe(B)/MgO MTJs. More information about MTJs with MgO barriers can be found in Sec. 4.2.

2.3. Current-voltage characteristics

A straightforward approach to characterize MTJs is to measure the current I as a function of the applied bias voltage V, i.e., an I/V curve. This voltage shifts the Fermi level of one electrode by eV as indicated in Fig. 2.2. Theoretically, the tunneling current through a symmetric potential depending on the bias voltage is described by the model of Simmons, which is described in the next section.

2.3.1. The Simmons model

The model of Simmons describes the current density through a symmetric tunnel barrier with similar electrodes [27]. It is based on the tunneling probability of each energy state, which is calculated with the transmission coefficient $T(E_\mathrm{x})$ within the free electron model. Additionally, Fermi functions $f(E)$ indicate whether the relevant energy state is occupied and if it has a free energy state in the second electrode to tunnel to. Since electrons are fermions, each energy state is occupied with two electrons

with antiparallel spin, resulting in a factor of 2. All in all, the current density J related to an applied bias voltage V can be expressed as

$$J = \int_0^{E_m} T(E_x)\mathrm{d}E_x \cdot \left(\frac{4\pi \mathrm{m}^2}{h^3} \int_0^{\infty} [f(E) - f(E + eV)]\,\mathrm{d}E_r \right), \tag{2.2}$$

where E_m is the maximum energy of the electrons, E_r is the energy of the electrons in polar coordinates, m is the mass of the electrons and h is Planck's constant. Here, eV represents the applied bias voltage. Within the Wentzel-Kramers-Brillouin (WKB) approximation, the transmission coefficient becomes

$$T(E_x) = \exp\left(-\frac{2}{\hbar}\right) \int_0^{d} \sqrt{2m(V(x) - E_x)\mathrm{d}x}, \tag{2.3}$$

with the potential $V(x)$, the barrier thickness d, the reduced Planck constant $\hbar$ and the energy E_x of the electron in x direction.

In general, the WKB approximation is applicable if the change of the potential $\frac{\mathrm{d}V}{\mathrm{d}x}$ in the range of one wavelength λ is small in comparison to

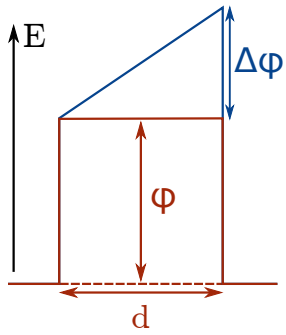

Figure 2.4.: Barrier parameters used in the models of Simmons [27] and Brinkman [28]. The red part with the barrier height φ (mean barrier height $\overline{\varphi}$ in the Simmons model) and the barrier thickness d are present in both models, while the blue part is the barrier asymmetry $\Delta\varphi$, introduced by Brinkman.

the kinetic energy E_{kin} [29]. The typical MTJ structures used in this work meet this requirement. More details about the WKB approximation are found in the Appendix V.

In the next step, Simmons replaces the arbitrary potential $V(x)$ with a mean barrier height according to

$$\bar{\varphi} = \frac{1}{d} \int_0^d \varphi(x) \mathrm{d}x, \tag{2.4}$$

where $\varphi(x)$ is the barrier height. Figure 2.4 illustrates this mean barrier height. By adding an auxiliary factor β, Simmons is able to integrate Eq. (2.2) and calculate the current density with the aforementioned approximations at $T = 0\,\mathrm{K}$ to be

$$J = \frac{e}{2\pi h(\beta d)^2} \left[\varphi \exp\left(-A\varphi^{\frac{1}{2}}\right) - (\varphi + eV) \exp\left(-A\left(\varphi + eV\right)^{\frac{1}{2}}\right) \right], \tag{2.5}$$

with $A = \frac{4\pi\beta d\sqrt{2m}}{h}$ and $\beta \approx 1$.

2.3.2. The Brinkman model

Often, the Simmons model was not able to quantitatively describe measured I/V curves. Thus, Brinkman et al. calculated the tunneling current depending on an applied bias voltage for an asymmetric barrier, which is not included in the model of Simmons because of the mean potential introduced in Eq. (2.4) [28]. Figure 2.4 shows the additional barrier asymmetry $\Delta\varphi$ with regard to the model of Simmons. In the Brinkman model, the barrier potential is set to

$$\varphi(x,V) = \varphi_1 + \frac{x}{d}\left(\varphi_2 - eV - \varphi_1\right), \tag{2.6}$$

with the barrier height φ_1 andφ_2 of electrode 1 and 2 and the direction of the current flow x. Brinkman calculates the numerical solution (current

density in A/cm^2) to Eq. (2.2) with the asymmetric potential within the WKB approximation to be

$$J = 3.16 \cdot 10^{10} \frac{\varphi^{\frac{1}{2}}}{d} \exp\left(-1.025\,\varphi^{\frac{1}{2}}\,d\right) \cdot \left[V - \frac{A_0\,\Delta\varphi}{32\,\varphi^{\frac{3}{2}}}\,e\,V^2 + \frac{3\,A_0^2}{128\,\varphi}\,e^2\,V^3\right], \tag{2.7}$$

with $A_0 = \frac{4\,d\sqrt{2\,m_{\text{eff}}}}{3\,\hbar}$. φ is the barrier height (in V), d is the thickness of the barrier (in Å), $\Delta\varphi$ is the barrier asymmetry (in V) and m_{eff} is the effective electron mass (in kg).

Figure 2.5 visualizes Eq. (2.7) with the influences of (a) the barrier asymmetry, (b) the barrier thickness and (c) the barrier height on the final $\mathrm{d}I/\mathrm{d}V$ or I/V curve, respectively. Clearly, the resulting $\mathrm{d}I/\mathrm{d}V$ and I/V curves are very sensitive to all three parameters.

In general, the error of the Brinkman model is $\leq 10\,\%$ if $\Delta\varphi/\varphi < 1$ and $d > 10\,\text{Å}$. The characteristic barrier parameters are deduced via [30]

$$\varphi^2 = \frac{e^2\,C}{32\,A}\ln^2\left(\frac{h^3}{\sqrt{2}\,\pi\,e^3\,m_{\text{eff}}}\sqrt{A\,C}\right),$$

$$d = -\frac{\hbar}{\sqrt{8\,\varphi\,m_{\text{eff}}}}\ln\left(\frac{h^3}{\sqrt{2}\,\pi\,e^3\,m_{\text{eff}}}\sqrt{A\,C}\right),$$

$$\Delta\varphi = -\frac{12\,\hbar}{e\sqrt{2\,m_{\text{eff}}}}\frac{\varphi^{\frac{3}{2}}}{d}\,\frac{B}{C}, \tag{2.8}$$

where A, B and C are fit parameters of the differential conductance defined as $\mathrm{d}J/\mathrm{d}V = AV^2 + BV + C$. Usually, the extracted barrier parameters are physically reasonable up to a bias voltage of $\approx (300 \text{ to } 500)\,\text{mV}$. Qualitatively, the asymmetric barrier results in a shift of the minimum of the $\mathrm{d}J/\mathrm{d}V$ curve along the voltage axis. This behavior can not be described with the Simmons model and is often observed experimentally.

The Brinkman model does not include band structure related effects, such as half-metallic ferromagnetism, and symmetry filter effects, such

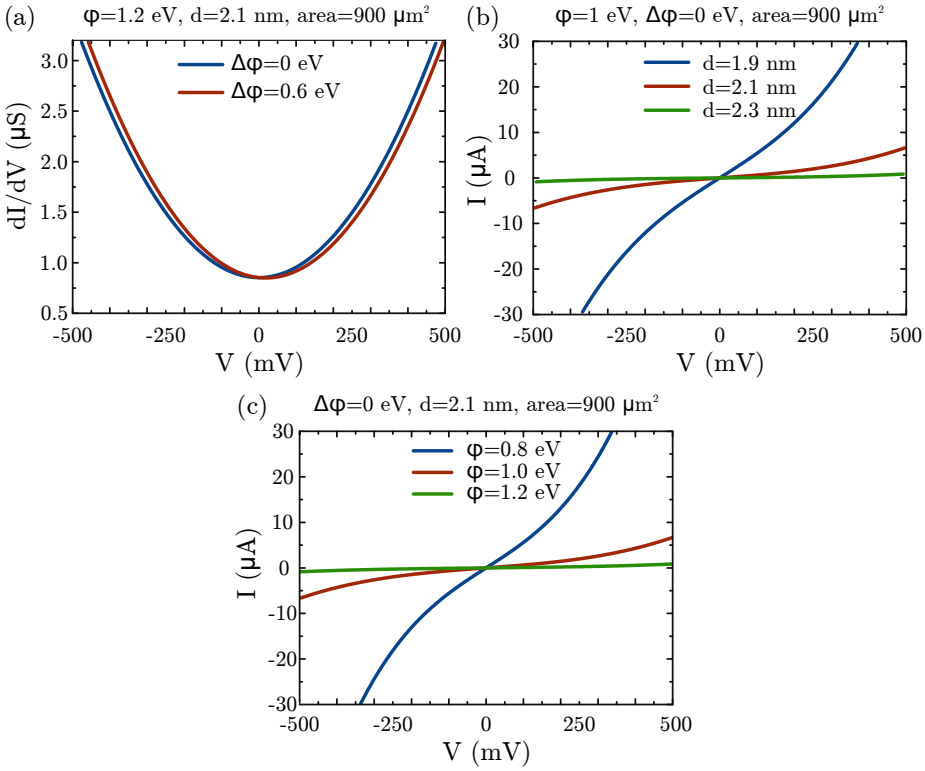

Figure 2.5.: (a) Influence of different barrier asymmetries on the minimum of the dI/dV curve. (b) Influence of different barrier thicknesses and (c) barrier heights on the I/V curve. The other Brinkman parameters are summarized at the top of each graph.

as the Δ_1 symmetry filter effect, which is responsible for the high TMR ratios in CoFeB/MgO MTJs (see Sec. 2.2). Since the MAO MTJs in this work exhibit TMR ratios well below 40 %, the Brinkman model is applicable.

3. The tunnel magneto-Seebeck effect

The theory of the TMR effect provides a profound understanding of electrons tunneling through a thin insulating barrier separated by two ferromagnetic electrodes if a bias voltage is applied. If this bias voltage is replaced by a temperature difference ΔT, a voltage V is generated according to the Seebeck effect via $V = -S\Delta T$. Here, S is the Seebeck coefficient, which is strongly material dependent. In general, the Seebeck coefficient of an MTJ depends on the magnetization alignment of the electrodes. Thus, different voltages are measured in the parallel and antiparallel orientation, respectively. This difference is referred to as the TMS ratio. In the following, the basic principles of the TMS effect are explained, starting with the normal Seebeck effect.

3.1. The Seebeck effect

Thomas Johann Seebeck studied the conversion of heat into electricity in 1821 and, as a result, launched the research field of thermoelectricity. Today, the so called Seebeck effect is well understood and measured for lots of materials. In general, every conducting material shows a Seebeck effect with a corresponding Seebeck coefficient. However, it is only possible to measure the Seebeck coefficient in relation to a second material, because the measurement wires exhibit a Seebeck effect as well, which leads to parasitic voltages. If the Seebeck coefficient of the second material is known, the absolute temperature or the corresponding Seebeck coefficient can be deduced when all other quantities are known. This device is called a thermocouple, which is widely used as a temperature sensor in both research and industry.

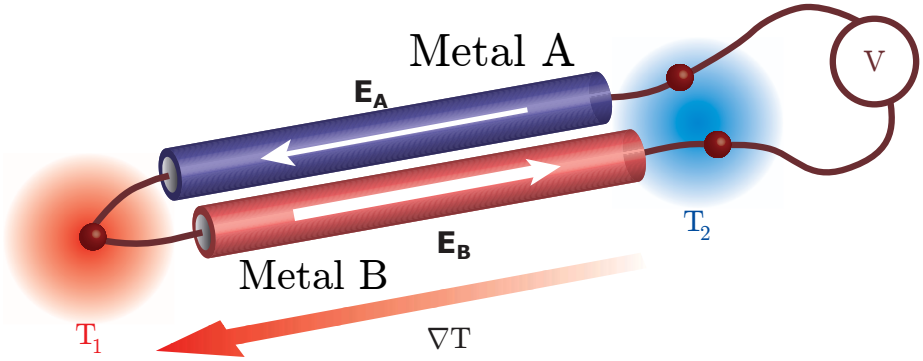

Figure 3.1.: Thermoelectric circuit with two metals A and B and temperatures T_1 and T_2. The influence of different Seebeck coefficients $S_{\mathrm{A,B}}$ on the electric field E is indicated by the thickness and the direction of the white arrows. Adopted from Ref. [8].

The basic principle of the Seebeck effect is schematically shown in Fig. 3.1. An electric field $E_{\mathrm{A,B}}$ builds up in the two metals A and B, which are subject to a temperature gradient ∇T with $\mathrm{T}_1 > \mathrm{T}_2$, according to

$$E_{\mathrm{A,B}} = -S_{\mathrm{A,B}} \cdot \nabla T, \tag{3.1}$$

where $S_{\mathrm{A,B}}$ denotes the Seebeck coefficient of material A and B. This electric field is a result of the temperature dependent diffusion of charge carriers. At the cold end (T_2), the charge carriers are moving more slowly in comparison to the charge carriers located around the hot end (T_1). Thus, an effective charge carrier motion towards the cold end is observed. In case of an open circuit, the resulting thermovoltage V can be expressed via

$$V = (S_{\mathrm{B}} - S_{\mathrm{A}}) \cdot (T_1 - T_2)\,. \tag{3.2}$$

Obviously, no voltage is measurable if $S_{\mathrm{A}} = S_{\mathrm{B}}$ (e.g. material A = material B). To measure an absolute temperature with a thermocouple,

the two Seebeck coefficients of the materials have to be known, one junction is kept at a reference temperature and the resulting Seebeck voltage is measured.

The assumption of electrons moving with different mean velocities due to the temperature difference is again based on the Drude-Sommerfeld model. It assumes the electrons to behave like a Fermi gas. However, experiments reveal positive as well as negative Seebeck coefficients. These findings are not explainable with the Drude-Sommerfeld model, because it does not include the band structure and the corresponding DOS of the material [31].

In a p-type semiconductor, for example, the diffusion current is mainly carried by holes, which leads to a positive S. In contrast, an n-type semiconductor exhibits a negative S, resulting in a voltage with opposite sign. If multiple p-type and n-type materials are cascaded together and a temperature difference is applied, the resulting device is called a Peltier cell, which can be used as a thermoelectric generator based on the Seebeck effect. However, due to the high costs and low efficiencies, the reciprocal effect of the Seebeck effect is often utilized in Peltier cells. This reciprocal effect is called the Peltier effect and describes an electrical current, which generates a temperature difference. If one side of the Peltier cell is kept at a constant temperature and a current is driven through the structure, the other side is effectively cooled or heated, respectively.

Since the DOS plays a vital role in the aforementioned effects, it is explained in more detail with regard to the Seebeck effect.

3.2. Sign and size of the Seebeck effect

The density of electrons with an energy E close to the chemical potential μ is given by the DOS $D(E)$ multiplied by the Fermi-Dirac statistic $f(E)$

$$n(E) = D(E)f(E) = D(E)\frac{1}{1+\exp\left(\frac{E-\mu}{k_\mathrm{B}T}\right)}, \tag{3.3}$$

with the Boltzmann constant k_B and the temperature T. Figure 3.2(a) shows the Fermi function for three different temperatures. At $T = 0\,\mathrm{K}$,

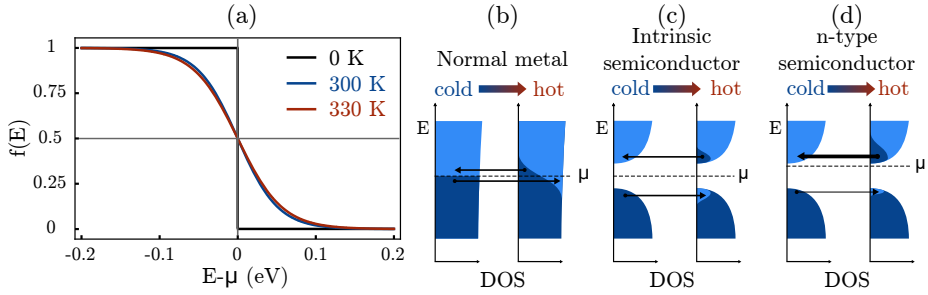

Figure 3.2.: (a) Fermi function for 0 K, 300 K and 330 K. (b) Schematic DOSs for a normal metal and (c) an intrinsic semiconductor. Currents from the hot to the cold side cancel out, because the density of occupied states above is similar to the density of empty states below the chemical potential μ. (d) An n-type semiconductor shows a large net current from the hot to the cold side due to the asymmetry of states above and below μ. In this picture, large Seebeck coefficients are only expected for the n-type semiconductor. Partly adopted from Ref. [32].

the Fermi function resembles a step function and the chemical potential is equal to the Fermi energy, i.e. $\mu = E_F$. Elevated temperatures lead to a gradual curvature increase of the Fermi function and states above μ are occupied.

In Figs. 3.2(b) to (d), three exemplary DOSs around μ are depicted for a normal metal, an intrinsic semiconductor and a p-type semiconductor in the presence of a temperature difference. At the hot sides, above μ, electrons are able to travel to the empty states at the cold sides ($T = 0$ K). Simultaneously, electrons below μ flow from the occupied states at the cold sides to the unoccupied states at the hot sides. Thus, two competing currents are present, which cancel out in the case of a normal metal and an intrinsic semiconductor (Figs. 3.2(b,c)). Accordingly, the expected Seebeck coefficients and voltages are small.

If additional states are inserted into an intrinsic semiconductor a few meV below the conduction band, for example via doping, the temperature

at the hot end results in an excess of electrons in the conduction band. This imbalance entails a large current from the hot to the cold side, while the current from the cold to the hot side is still small. Hence, a large net current flows from the hot to the cold side implying a large Seebeck coefficient, which is visualized in Fig. 3.2(d). The sign of the Seebeck coefficient directly determines the carrier type, i.e., if the current flow is dominated by electrons or holes.

Please note, that in real systems the carrier mobility depends on the temperature and can intrinsically be very different for electrons and holes (e.g. 1400 $\frac{\mathrm{cm}^2}{\mathrm{Vs}}$ for electrons versus 450 $\frac{\mathrm{cm}^2}{\mathrm{Vs}}$ for holes in Si at 300 K [33]). However, the aforementioned principles are sufficient to explain the sign and size of the Seebeck effect on a basic level. With the general understanding of the TMR and Seebeck effect, the TMS effect, which combines both effects in nano-sized structures, is described in more detail in the next section.

3.3. Theory of the tunnel magneto-Seebeck effect

In principle, the TMS effect describes the dependence of the Seebeck coefficient of an MTJ on the magnetic orientation of the two ferromagnetic electrodes. Therefore, different voltages are measured in the parallel and antiparallel state if the MTJ is subject to a temperature gradient. Similar to the TMR ratio (cf. Eq. (2.1)), the TMS ratio is defined as

$$\mathrm{TMS} = \frac{S_\mathrm{p} - S_\mathrm{ap}}{\min\left(|S_\mathrm{p}|,|S_\mathrm{ap}|\right)}, \tag{3.4}$$

where $S_\mathrm{p,ap}$ is the Seebeck coefficient in the parallel, antiparallel magnetization configuration. With $V_\mathrm{p/ap} = -S_\mathrm{p/ap}\Delta T$ this equation can be rewritten to

$$\mathrm{TMS} = \frac{V_\mathrm{ap} - V_\mathrm{p}}{\min\left(|V_\mathrm{ap}|,|V_\mathrm{p}|\right)}, \tag{3.5}$$

with the experimentally observed voltages $V_\mathrm{p/ap}$ in the parallel/antiparallel state. The principal idea is pictured in Fig. 3.3.

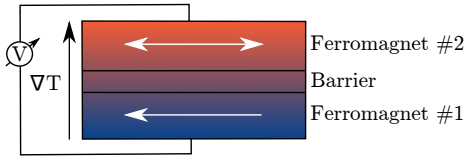

Figure 3.3.: Schematic concept of the TMS. A temperature gradient ∇T across an MTJ results in different voltages for parallel and antiparallel magnetization alignment due to the changing Seebeck coefficient of the MTJ.

Like in Sec. 3.1, a detailed look at the involved DOSs is able to explain the occurrence of different voltages. Figures 3.4(a,b) show the spin resolved currents emerging in an MTJ, if one ferromagnet (FM) is heated. In the antiparallel state, a lot of electrons are available below μ on the cold side, while only a few states are available below μ on the hot side. At the same time, electrons above μ tunnel from the hot side to the cold side. Overall, both contributions are of the same order and the resulting Seebeck coefficients and, thus, the voltages are small.

In contrast, more final states are available for the electrons above μ in the parallel state in comparison to the antiparallel state. Hence, a net current flows from the hot to the cold end of the MTJ, resulting in a high voltage and Seebeck effect. This simple picture was verified for CoFeB/MgO MTJs by Walter et al. [12]. They measured an antiparallel Seebeck coefficient of $S_{\mathrm{ap}} = -99.2\,\mu\mathrm{V/K}$ and a parallel Seebeck coefficient of $S_{\mathrm{p}} = -107.9\,\mu\mathrm{V/K}$, resulting in a TMS ratio of $-8.8\,\%$.

However, the DOSs shown in Fig. 3.4 do not include more complicated band structure features like, for example, gaps or peaks. In addition, no assumption is made about the tunneling barrier and its influence on the tunneling process (see Sec. 2.2 for more details). To take these properties into account as well, a more sophisticated theoretical approach is needed. One possibility is the utilization of the bottom-up Landauer-Büttiker formalism in the ballistic transport regime [34].

This concept assumes two contacts with Fermi functions f_{L} and f_{R} separated by a transport channel with an energy dependent transmission $T(E)$. Since the transport of electrons through tunnel barriers in MTJs

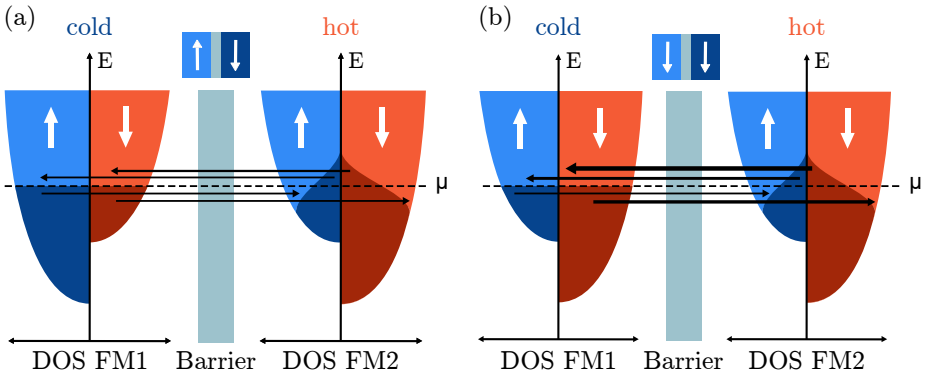

Figure 3.4.: (a) Schematic DOS for cold and hot side of the ferromagnets in the antiparallel state. (b) Schematic DOS for cold and hot side of the ferromagnets in the parallel state. The thickness of the arrows represents the current strength. A high voltage and a high Seebeck coefficient is expected in the parallel case only. Adopted from Ref. [32].

is dominated by elastic processes, the length of the transport channel is assumed to be short in comparison to the mean free path of the electrons, enabling ballistic transport. Figures 3.5(a,b) depict the resulting Fermi functions of applying either (a) a bias voltage or (b) a temperature difference to the contacts and the difference in occupation at the left and right contact $f_\mathrm{L} - f_\mathrm{R}$.

In case of an applied bias voltage and a constant base temperature, the occupations are shifted along the energy axis (Fig. 3.5(a)). Effectively, the electrons flow from the left to the right contact, giving rise to a current in a closed circuit geometry. As only electrons within the interval between $f_\mathrm{L} - f_\mathrm{R}$ contribute, the total net current, weighted by $T(E)$, is

$$I = \frac{2e}{h} \int \mathrm{d}E \, (f_\mathrm{L} - f_\mathrm{R}) \, T(E). \tag{3.6}$$

This result is universal as long as the ballistic assumption is valid and the occupation function and transmission are known.

With an applied temperature difference across the device though, as

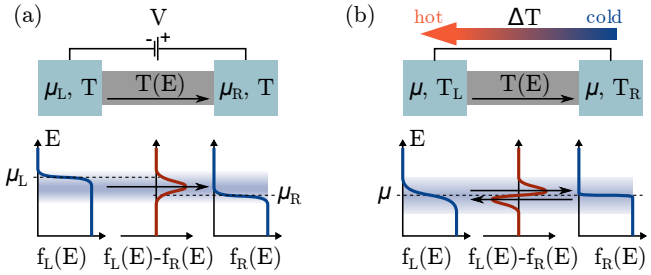

Figure 3.5.: (a) Schematic Landauer model with chemical potentials μ_L and μ_R at the left and right contact, respectively. (b) Landauer model with different temperatures of the left (T_L) and the right (T_R) contact. $T(E)$ is the transmission along the transport channel. Adopted from Ref. [32].

seen in Fig. 3.5(b), the Fermi functions smear out differently (cf. Fig. 3.2), while μ stays the same in both contacts. Similar to the case with an applied voltage, an occupation difference $f_L - f_R$ is observed. Since $T(E)$ is energy dependent, the contributions to the net current of the electrons below and above μ do not cancel out. In addition, $T(E)$ depends on the DOS of the used material and the electronic processes inside the barrier. Thus, the Landauer-Büttiker formalism provides an improved theory to deal with real systems such as MTJs.

Several groups use ab initio calculations based on the Landauer-Büttiker formalism to deduce thermoelectric properties of nano-sized structures. Important during these calculations is the usage of small voltages and temperature differences, which allows the current to be calculated within the linear response regime via

$$I = (\Delta\mu/e + S\Delta T) \cdot G, \tag{3.7}$$

with the difference of the chemical potentials $\Delta\mu$ and the conductance G. Together with the linearized form of Eq. (3.6) the conduction G is given via

$$G = -\frac{e^2}{h} \int \mathrm{d}E \left(\frac{\partial f}{\partial E} \right) T(E), \tag{3.8}$$

and the Seebeck coefficient via

$$S = -\frac{1}{eT} \frac{\int \mathrm{d}E \left(\frac{\partial f}{\partial E} \right) (E - \mu)\, T(E)}{\int \mathrm{d}E \left(\frac{\partial f}{\partial E} \right) T(E)}. \tag{3.9}$$

The area enclosed by $\mathrm{d}E \left(\frac{\partial f}{\partial E} \right) T(E)$ is proportional to the conductance, with $\mathrm{d}E \left(\frac{\partial f}{\partial E} \right)$ being the thermal broadening of the Fermi function as described in Sec. 3.2. Only the states within this interval contribute to the transmission. A closer look at Eq. (3.9) reveals that the Seebeck coefficient S is the geometric center of the aforementioned area.

Figures 3.6(a,b) visualize the physical implications of Eqs. 3.8 and 3.9. Here, the light colored area represents the transmission of the MTJ, i.e. $\mathrm{d}E \left(\frac{\partial f}{\partial E} \right) T(E)$, in the p and ap state, respectively. Furthermore, the light blue colored bar is the geometric center, i.e., the Seebeck coefficient. In the case of Fig. 3.6(a), a high difference of the transmissions between the p and ap state is pictured, which leads to a high TMR effect. However, the difference between the Seebeck coefficients is marginal and, thus, a low TMS ratio is expected. Compared to Fig. 3.6(b), the transmissions experience a high difference again, but the geometric centers are asymmetrically centered around μ. Hence, a high TMR as well as a high TMS ratio is obtained. In general, a high TMR effect does not entail a high TMS effect.

Heiliger et al. used Eqs. (3.8) and (3.9) in combination with ab initio methods to study spin caloritronic effects in CoFe/MgO MTJs depending on the temperature [11], to determine the influence of the magnetic material, i.e., the composition of CoFe electrodes, on the TMS effect [35] and to analyze thermoelectric properties of ZnO-based super-lattice structures [36]. Additionally, thermoelectric properties of MTJs with half-metallic Heusler electrodes were investigated [37, 38].

Further theoretical work was done by Lopez-Monis et al., who inspected junctions with a ferromagnet and a normal metal separated by

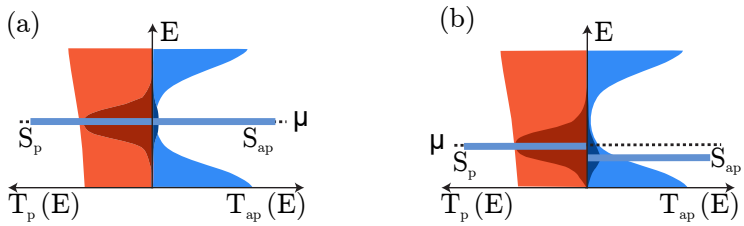

Figure 3.6.: (a) Symmetric transmissions of an MTJ in the p and ap state. The resulting low difference between the Seebeck coefficients leads to a low TMS effect. (b) Asymmetric transmission of an MTJ, which promote a high TMR and a high TMS. The light blue and red areas represent the transmission in the p and ap state, while the light blue bar symbolizes the geometric center of the dark areas, which corresponds to the Seebeck coefficient. Adopted from Ref. [32].

a semiconductor [39] as well as MTJs [40]. A combination of theoretical predictions and experimental measurements was demonstrated by Walter et al. [12]. Generally, the trends predicted by the Landauer-Büttiker formalism are qualitatively verified by the experiments. However, since the simulations are based on perfect structures and interfaces, a quantitative difference between theory and experiment is often observed.

In the following, different ways of experimentally generating a temperature difference inside an MTJ are presented.

3.4. Measuring the tunnel magneto-Seebeck effect

In order to generate a temperature difference across the thin insulating barrier of an MTJ, two experimental methods have been established in recent years, namely the laser-induced and the extrinsic heating method. The fact that the first publications of both methods have been published just within a short time period demonstrates the huge interest associated with thermovoltages in MTJs. In addition, a relatively new, third model suggested the extraction of Seebeck coefficients from analyzing the symmetry of V/I curves, without the use of any external heating sources.

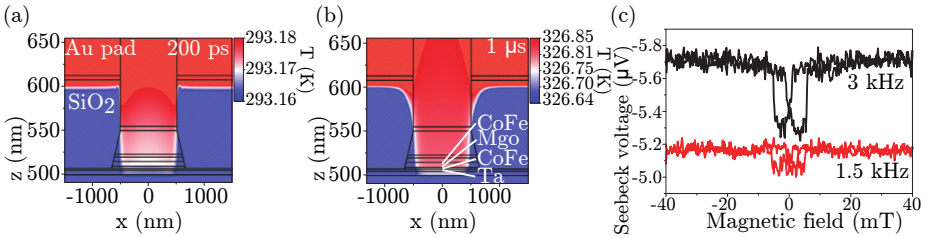

Figure 3.7.: (a,b) COMSOL simulations of temperature distributions across the MTJ 200 ps and 1 μs after the laser is directed to the Au pad. (c) Typical TMS measurement for two lock-in modulations. Adopted from Ref. [12].

Therefore, this third method is called the intrinsic model. The majority of the experiments is done with CoFeB/MgO MTJs. All three methods together with their corresponding model are discussed in the following.

Laser-induced tunnel magneto-Seebeck effect

The first experimental observation of the TMS effect was in 2011 by Walter et al. [12]. They used a focused laser beam with a diameter of (15 to 20) μm and a laser power of 30 mW to heat the top of an MTJ, which consisted of CoFeB electrodes and an MgO barrier of 2.1 nm. The energy of the laser is absorbed by the Au pad on top of the MTJ, which is shown in Figs. 3.7(a,b) for 200 ps and 1 μs after the laser beam is turned on. In addition, the thick substrate on the bottom functions as cooling reservoir, which results in the formation of a temperature difference across the MTJ.

A typical TMS measurement with this setup is shown in Fig. 3.7(c) for two lock-in modulations. Here, the area, which is heated by the laser, is increased due to the slower modulation of the laser. Thus, the contribution of the Seebeck voltage at the junction decreases as well as the overall signal. The thermovoltages and the Seebeck coefficients measured by Walter et al. agree qualitatively very well with theoretical predictions also presented in their work.

A follow-up study investigated the time dependence of the TMS effect

and found parasitic effects originating from semiconducting substrates such as Si [41], which were independently confirmed by Xu et al. [42]. Thus, in the work at hand, only MgO substrates are used. Very large TMS ratios of $\approx 3000\,\%$ were realized with an additionally applied bias voltage [43]. With this bias voltage, it is possible to effectively move the chemical potential, directly influencing the states responsible for the TMS effect (cf. Fig. 3.4).

In order to further increase the effect sizes and the thermovoltages, half-metallic Heusler electrodes such as Co_2FeSi were used in combination with MgO barriers [44]. Here, the n-type gap in the spin-down DOS and the metallic behavior in the spin-up DOS of Co_2FeSi results in large Seebeck voltages ($> 600\,\mu V$) and high TMS ratios ($\approx 100\,\%$) in contrast to MTJs with CoFeB electrodes ($\approx 90\,\mu V$ and (30 to 50) %).

Extrinsic tunnel magneto-Seebeck effect

A second method to generate temperature differences inside an MTJ makes use of Au heater lines (HLs). The HLs are patterned on top of the MTJ with an additional lithography step. By driving an ac or dc current through the Au, Joule heating heats up the MTJ from the top and creates a temperature difference due to the substrate again acting as cooling reservoir. Therefore, a thermovoltage can be measured depending on the external magnetic field. Since the HL is electrically isolated from the MTJ via a 160 nm thick Ta_2O_5 film, this method is called the extrinsic TMS. The basic principle is visualized in Fig. 3.8. With this setup, Liebing et al. [13, 45–47] measured the thermopower depending on the applied heating power, deduced Seebeck coefficients of CoFeB/MgO based MTJs, investigated the resulting thermocurrents and conducted noise spectroscopy measurements. The resulting thermovoltages of up to $100\,\mu V$ and TMS ratios of up to $50\,\%$ correspond very well to the results of the laser-induced TMS.

Böhnert et al. focused on the implementation of integrated thermometers to gain insight into the actual thermal distribution inside an MTJ [48]. In addition, they used an MgO wedge resulting in a barrier thickness ranging from 1.2 nm to 1.6 nm, without finding any systematic

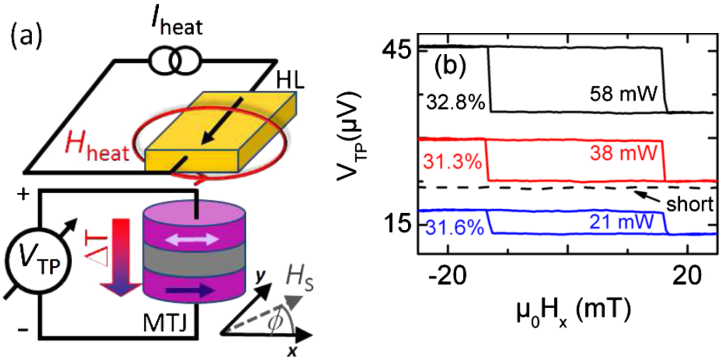

Figure 3.8.: (a) Basic measurement configuration with the MTJ and the HL on top. I_{heat} creates the temperature gradient across the MTJ. (b) Measurements of the thermovoltage depending on the magnetic field for different applied heating powers. Taken from Ref. [13].

correlation between the thermovoltage and the barrier thickness. Again, the thermovoltages and the TMS ratios are in the range of several tens of μV and %, respectively. Another study focused on the influence of the thermal interface resistance on the thermovoltage of an MTJ [49]. This publication along with others lead to a fervent discussion about the actual thermal conductivity of thin films, which is summarized in Sec. 5.3. The reciprocal effect to the TMS effect, the magneto-Peltier effect, was measured with the measurement geometry of the extrinsic TMS as well [50]. In addition, thermal spin current injection from a ferromagnet to silicon via a tunnel barrier was demonstrated [51].

Intrinsic tunnel magneto-Seebeck effect

Zhang et al. and Teixeira et al. [52,53] proposed a method to extract the Seebeck coefficients of MTJs which uses the direct intrinsic Joule heating of the tunneling current generated by a bias voltage to create the temperature difference inside the MTJ and is, therefore, called the intrinsic TMS. With a model of a Thomson thermoelectric conductor (TTC), the Onsager reciprocal relations and the energy conservation principle, they

end up at

$$\mathbf{J} = -(\sigma/e^2)\nabla\overline{\mu} + (S\sigma/|e|)\nabla T,$$

$$\mathbf{J}_\mathrm{Q} = (TS\sigma/|e|)\nabla\overline{\mu} - (\kappa + TS^2\sigma)\nabla T,$$

$$C_\mathrm{v}\partial T/\partial t + \nabla\cdot\mathbf{J}_\mathrm{W} = 0, \tag{3.10}$$

with the total energy flux density $\mathbf{J}_\mathrm{W} = \mathbf{J}_\mathrm{Q} + \overline{\mu}\mathbf{J}$. $\overline{\mu} = \mu - \mathrm{eV}$ is the electrochemical potential, $\mathrm{C_v}$ is the specific heat per unit volume, σ is the electric conductivity, κ is the thermal conductivity, T is the temperature, S is the Seebeck coefficient and e is the electron charge.

In case of an asymmetric TTC and at steady state conditions ($\partial T/\partial t = 0$), Zhang et al. [52] solve Eq. (3.10) to

$$V(I) = R\cdot I + S\cdot\sum(\eta_\mathrm{j}R_{\kappa\mathrm{j}}R_\mathrm{j})\cdot I^2, \tag{3.11}$$

with the resistance $R \equiv \sum R_\mathrm{j}$ of the junction and the Seebeck coefficient $S \equiv \sum(\eta_\mathrm{j}R_{\kappa\mathrm{j}}R_\mathrm{j}S_\mathrm{j})/\sum(\eta_\mathrm{j}R_{\kappa\mathrm{j}}R_\mathrm{j})$ of the MTJ. $R_\mathrm{j} = d_\mathrm{j}/(\sigma_\mathrm{j}A)$ is the resistance, A is the area of the MTJ, d_j is the thickness of the junction, $R_{\kappa\mathrm{j}}$ is the heat resistance, $\eta_\mathrm{j} = (T_1 - T_0)/T_\mathrm{m}$ is the thermal asymmetric parameter with the mean temperature T_m and the temperature T_0,T_1 of the reservoir 0,1 and S_j is the absolute thermopower. The parameter j denotes the j-th layer.

Furthermore, they state that with Eq. (3.11) it is directly possible to extract the Seebeck coefficient of an MTJ via the second-order contribution to the voltage without using any external heating sources. The corresponding experiment combines dc transport measurements with an additionally applied magnetic field to control the magnetization alignment of the two ferromagnetic electrodes. A current is sent through the MTJ with positive and negative polarity, resulting in voltages $\mathrm{V_+}$ and $\mathrm{V_-}$, respectively.

With Eq. (3.11) the symmetric and antisymmetric voltage contributions are calculated via $(V_+ + V_-)/2 = S\cdot\sum(\eta_\mathrm{j}R_{\kappa\mathrm{j}}R_\mathrm{j})\cdot I^2$ and $(V_+ -$

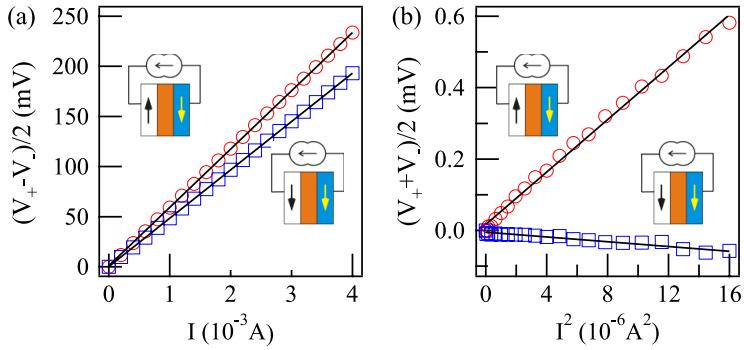

Figure 3.9.: Original data from Ref. [52] showing the linear fits to the antisymmetric (a) and symmetric (b) part of the V/I curve, which are used to extract the resistance and the Seebeck coefficient.

$V_-)/2 = IR$. In the picture of the intrinsic TMS, the antisymmetric contribution is plotted versus the current I in order to deduce the resistance R. Additionally, by plotting the symmetric part versus I^2, the Seebeck coefficient S is obtained via the slope of a linear fit, if $\sum(\eta_\mathrm{j} R_{\kappa\mathrm{j}} R_\mathrm{j})$, which depends on material parameters only, is known. In order to visualize this procedure, Figs. 3.9(a,b) show the original data from Ref. [52]. They are able to calculate large TMS ratios of more than 1000 %, which could not be verified with the laser-induced or the extrinsic method. Analyzing this discrepancy is part of the thesis at hand.

Part II.

Experiment

4. Materials

In this work, MTJs with different barrier materials (MAO and MgO, respectively) are compared in various ways. However, the overall MTJ structure involves several other important layers, which are presented in the next section. Furthermore, the necessary deposition and patterning processes are summarized and the role of MAO and MgO as barrier material is highlighted.

4.1. Fabrication of magnetic tunnel junctions

All layers are formed by sputter deposition, which is a popular deposition technique of thin films, in a Leybold Vakuum GmbH CLAB 600 cluster tool. This system has a base pressure below $5 \cdot 10^{-7}$ mbar in order to minimize the incorporation of impurities. The standard MTJ recipe consists of a bottom contact of Ta 10/Ru 30/Ta 5/Ru 5, an exchange biased MTJ of MnIr 10/$Co_{40}Fe_{40}B_{20}$ 2.5/barrier d_N/$Co_{40}Fe_{40}B_{20}$ 2.5 and a top contact of Ta 5/Ru 30 (all numbers are thicknesses in nm; d_N is the nominal thickness of the barrier). In case of the insulating barrier, rf sputtering is used while the other layers are deposited by dc sputtering. MAO, MgO, MnIr and CoFeB are sputtered from composite targets, Ta and Ru from elemental targets. Si substrates have been found to generate parasitic thermovoltages during TMS experiments due to their semiconducting properties, which is why insulating MgO (001) substrates are used [41]. Table 4.1 shows the resulting MTJs with MAO and MgO barrier thicknesses, respectively.

Figure 4.1(a) depicts the final schematic structure of the whole stack. In the following, the lower CoFeB layer is pinned via exchange bias of the underlying MnIr layer to achieve different switching fields of the ferromagnetic electrodes. For this activation of the exchange bias effect,

Table 4.1.: Overview of different nominal barrier thicknesses of each series.

Series	Nominal barrier thickness (nm)							
I (MAO)	1.0	1.4	1.6	1.8[a]	2.0[a]	2.2	2.6	3.0
II (MgO)	1.2	1.5	1.8	1.9	2.0	2.3	2.6	2.9

[a]Samples were prepared independently of the rest of the series.

the stack is heated to 350 °C for one hour and then cooled in an in-plane magnetic field of 0.7 T. Simultaneously, this post annealing process promotes the crystallization of the CoFeB electrodes. The incorporation of Ta is necessary, because the small B atoms start to diffuse at relatively low temperatures and, eventually, reach the MgO barrier, where they decrease the crystalline order and, thus, the TMR ratio. Therefore, Ta acts as B getter material, effectively leading to crystalline CoFe electrodes with high spin polarizations and smooth interfaces.

In the next step, the samples are patterned into elliptical MTJ pillars with the major axis in the exchange bias direction. This patterning process involves two electron beam lithography steps. After the first step, the redundant material between the elliptical pillars is removed via Ar etching up to the bottom contact. The etching process is monitored by secondary ion mass spectroscopy. In order to isolate the individual junctions electrically, 120 nm of Ta_2O_x is sputtered next to the freestanding ellipsoids. In a second lithography step, 5 nm of Ta and 60 nm of Au are deposited on the whole sample and patterned into bond pads to make electrical and optical access possible. The final geometry of the sample is schematically sketched in Fig. 4.1(b). C#/R# corresponds to the respective column/row number, which is continued to C9 and R5 in this specific template, resulting in a total of 180 MTJs per template. Usually, two templates are patterned onto one sample.

A scanning electron microscope image of one segment of the final sample is shown in Fig. 4.1(c). Here, the four individual MTJs are clearly visible. Additionally, an old Au bond is identifiable on the top left bond pad. Clearly, the bond is well away from the MTJ to exclude parasitic

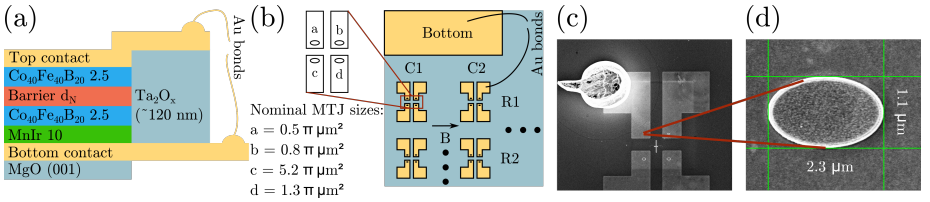

Figure 4.1.: (a) Schematic view of the final layer sequence. (b) Sample geometry from the top with different junction sizes and columns/rows. The direction of the exchange bias is indicated by the arrow. (c) Scanning electron microscope image (268 x, 10 kV) of one segment with four MTJs. An old Au bond is visible on the top left bond pad and a cross in the middle of the structure, which is used as visual feedback. (d) Magnified section of (c) with only one MTJ (27000 x, 10 kV) with an actual area of $0.6\,\pi\mu m^2$.

effects during the heating of the MTJ. By further zooming in, the actual size of the MTJs is obtained (Fig. 4.1(d)). In this case, a nominally $0.5\,\pi\,\mu m^2$ MTJ results in an actual area of $0.6\,\pi\,\mu m^2$. On average, the patterned MTJs are enlarged by about 20 % by the patterning process in comparison to the nominal MTJ area. This difference has to be taken into account during the data evaluation.

Lastly, the patterned samples are glued to a commercially available 24-lead ceramic package. The chip carrier is then connected to the top and bottom contact of one MTJ via thin Au bonding wires and transferred to the setup.

4.2. MgO and $MgAl_2O_4$ as tunnel barrier

Figure 4.2 shows the temporal progression of the TMR ratio. The first time, MgO based MTJs surpassed MTJs with an Al_2O_3 barrier dates back to 2004, where Parkin et al. [54] and Yuasa et al. [55] measured very high TMR ratios of up to 220 % at room temperature. Until then, amorphous Al_2O_3 based MTJs exhibited the highest TMR ratios of around

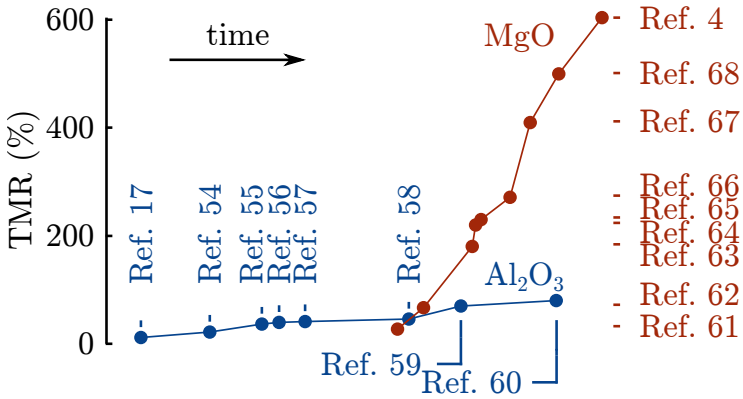

Figure 4.2.: Temporal evolution of the TMR ratio of MTJs with Al_2O_3 (Refs. [17, 56, 59–64]) and MgO (Refs. [4, 54, 55, 65–70]) barrier, respectively. Adopted from Ref. [71].

70 % [56]. However, higher TMR ratios could not be reached with amorphous Al_2O_3 barriers. Instead, MTJs with epitaxial Fe electrodes and crystalline MgO barriers were predicted to achieve switching ratios in the region of a few thousand percent [57, 58]. Soon, such a high TMR ratio was experimentally realized in CoFeB/MgO/CoFeB MTJs by the suppression of Ta diffusion, which occurred at high annealing temperatures and thin CoFeB electrodes, with 604 % at room temperature and more than 1000 % at low temperature [4]. Responsible for the high TMR ratios is the Δ_1 symmetry filter effect, which was explained in more detail in Sec 2.2.

MgO crystallizes in the cubic rock salt structure with a bulk lattice constant of 4.21 Å in the (001) direction. This structure leads to a lattice mismatch of (3 to 5) % with typically used cubic electrode materials such as Fe (2.87 Å). A direct consequence is the formation of misfit dislocations due to the induced strain. Bonell et al. [72] demonstrated that the misfit dislocation density strongly influences the TMR ratio. Another distinctive drawback of MgO is its hygroscopicity, complicating the handling in the lab.

Nevertheless, many groups focused on MTJs with MgO barrier because of their high TMR ratios and the relatively small computational

effort, making a direct comparison of experiment and theory possible. Although, MgO, with a bandgap of 7.8 eV [73], is well insulating, it shows a remarkably high bulk thermal conductivity of $\kappa \approx 50 \frac{\mathrm{W}}{\mathrm{K \cdot m}}$. The thermal conductivity of thin MgO films is further discussed in Sec. 5.3.

In the group of Reiss et al., MTJs with MgO barriers are used, for example, to characterize low temperature characteristics with inelastic electron tunnel spectroscopy (IETS) such as magnon or phonon excitations [75] or to improve the TMR ratio with half-metallic Heusler electrodes such as Co_2FeSi [76], which exhibits only a small lattice mismatch with respect to MgO and determines the growth direction at the same time [76]. Usually, the MgO barriers are either deposited by sputtering or electron beam evaporation, respectively. Furthermore, TMS measurements and calculations have been primarily done with MgO MTJs up to now, which were summarized and explained in Sec. 3.4.

MAO belongs to the spinel group, which consists of materials with a general formula of $A^{2+}B_2^{3+}O_4^{2-}$. In case of MAO, the oxide anions form

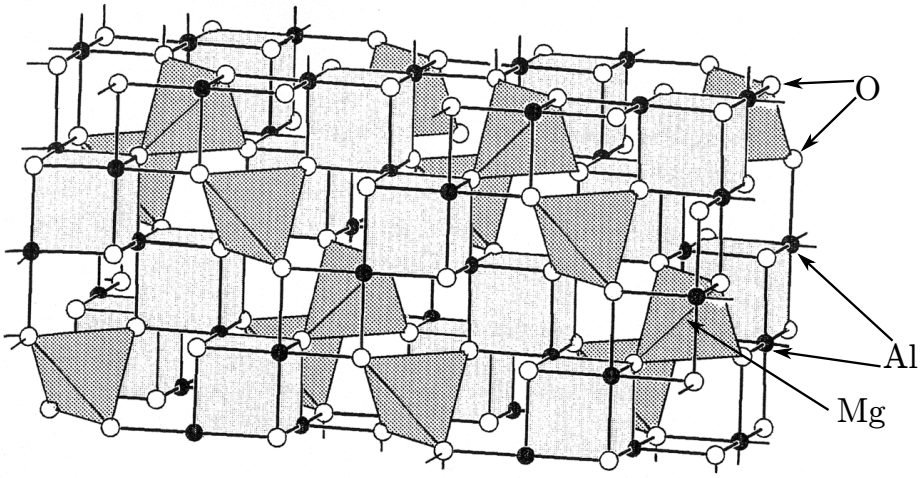

Figure 4.3.: Section of the MAO crystal structure. The black dots are Al atoms, the white dots are O atoms and the Mg atoms are in the center of the tetrahedrons spanned by the O atoms. Adopted from Ref. [74].

a cubic close-packed lattice, while the Mg^{2+} and Al^{3+} cations occupy the octahedral and tetrahedral sites (see Fig. 4.3). Accordingly, the conventional unit cell of MAO contains 56 atoms [77]. With this large unit cell, the computational time of standard DFT calculations is significantly increased in comparison to MgO with 8 atoms in the unit cell.

Nonetheless, several groups published experimental as well as theoretical studies about MAO as a barrier material in MTJs. Firstly, ab initio studies revealed that MAO shows a Δ_1 symmetry filter effect comparable to MgO [77, 78], which is even enhanced with an additional cation-site disorder [79]. Low-resistive MAO based MTJs showed magnetization switching via spin-transfer torque and an improved bias voltage dependence in comparison to MgO based MTJs [80]. Very high TMR ratios of 245 % at RT (436 % at 3 K) with Fe electrodes [81] and 342 % at RT (616 % at 4 K) with highly spin-polarized Co_2FeAl electrodes [82] were demonstrated.

Moreover, the low lattice mismatch between the MAO barrier and Fe electrodes resulted in pronounced resonant tunneling features in quantum well structures [83]. In this publication, MTJs with double MAO barriers exhibited an effect enhancement of one order of magnitude in comparison to MgO MTJs.

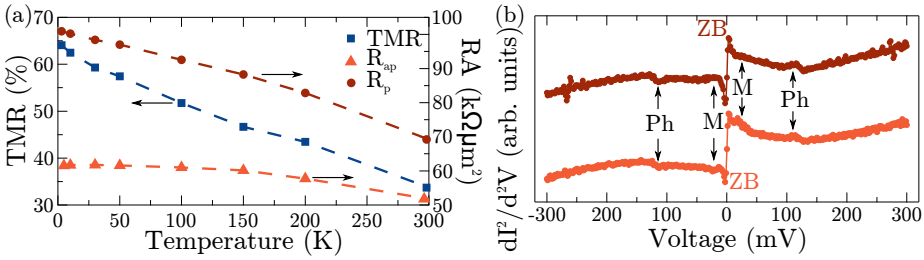

Figure 4.4.: (a) TMR and RA products depending on the temperature of an MAO based MTJ with a barrier thickness of 2.0 nm. (b) IETS spectra at 3 K for antiparallel (dark red) and parallel (light red) magnetization alignment. Curves are shifted horizontally for clarity. ZB is the zero bias anomaly and Ph and M denote the phonon and magnon excitations, respectively.

In our group, MTJs with MAO barrier started to attract more attention as an alternative to MTJs with MgO barrier only recently. A preceding study focused on the effect of different adhesive layers and the general improvement of interface structure [84]. The best roughness values were found by sputtering MAO from a composite target with maximum TMR values of around 35 % for a barrier thickness of 2.0 nm. Also, low temperature TMR and IETS measurements of MAO based MTJs were done (see Fig. 4.4). The results of the TMR, the RA product and the IETS measurements are in very good agreement with the outcomes obtained at similar MTJ systems by Tao et al. [85].

5. Methods

In the upcoming sections the used setup located in Greifswald is described in more detail. With this setup, it is possible to measure either TMR and I/V or TMS signals. Since the TMR and TMS experiments are slightly different, both are presented in detail. The setup is placed on an optical table (THORLABS Nexus) to ensure vibration isolation and an air conditioning system provides stable ambient conditions.

5.1. Setup for transport measurements

5.1.1. TMR and I/V measurements

Figure 5.1(a) presents a real image of the setup, which is used for the TMR, I/V and TMS measurements, respectively. Before mounting the sample, the carrier socket is connected to ground by a simple switch, thus preventing parasitic voltages from destroying the barrier. Additionally, coaxial cables connect the bonded pins to the measurement electronics. With the pole shoes in the direction of the short axis of the chip carrier, an electromagnet generates in-plane fields of $B = \pm 50\,\mathrm{mT}$ with a minimum step size of 0.2 mT in the direction of the major axes of the MTJ pillars. Thus, an additional shape anisotropy ensures an enhanced switching of the MTJs. By connecting a Keithley 2400 source meter to the bottom and top contact of the MTJ it is possible to measure the current I passing through the MTJ when applying a bias voltage V.

In this work, a bias voltage of 10 mV is used for all TMR measurements, while the I/V curves are subsequently measured with maximum bias voltages of $\pm 300\,\mathrm{mV}$ in steps of 1 mV in the parallel and antiparallel state. The resistance area (RA) product is used to compare MTJs with different areas or barriers (material and thickness) and is calculated from I and

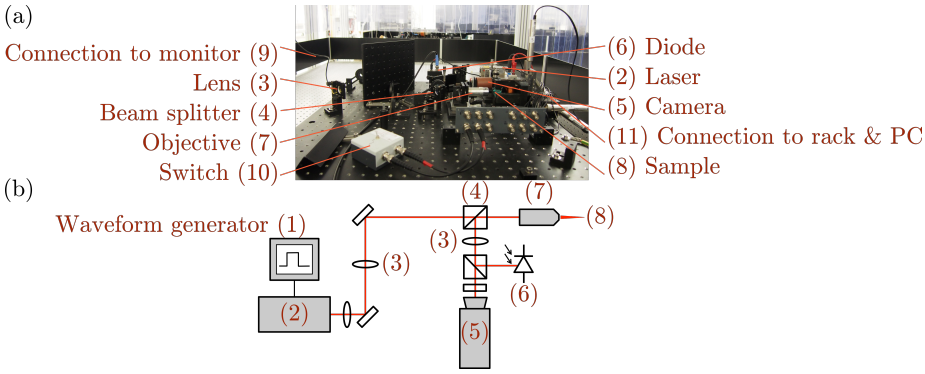

Figure 5.1.: (a) Real image of the setup that is used to measure the laser-induced TMS. (b) Schematic sketch of the setup and the beam path. The waveform generator (which is part of the measurement rack) is added to emphasize the laser modulation. Adopted from Ref. [86].

V ($R = V/I$) times the actual area A of the MTJ. TMR measurements in this setup are subject to an error of $< 1\,\%$.

5.1.2. TMS measurements

After measuring TMR and I/V characteristics, the sample is connected to ground in order to safely disconnect the TMR measurement electronics. For the TMS measurements, a precision voltage amplifier (Femto; DLPVA-100-F-S; DC mode at a gain of 60/80 dB (factor of 1000/10000), bandwidth of 100 kHz and input impedance of 1 TΩ) in combination with a lock-in amplifier (Stanford Research Systems SR830; time constant 100 ms and low noise reserve) is used. Additionally, an oscilloscope displays the temporal evolution of the Seebeck voltage.

Figure 5.1(b) shows the schematic path of the laser beam which is used to heat the MTJ on the top. A diode laser (Toptica iBeam smart 640-S) with a wavelength of $\lambda = 637\,\text{nm}$ and a power ranging from 1 mW to 150 mW is modulated with a rectangular signal via a waveform generator (Agilent 3352A) and focused through various optics onto the sample. In the focal plane, the laser has a beam waist of around $w_0 = 2\,\mu\text{m}$,

which is determined with the knife edge method (see Sec.5.2). The frequency of the modulation is freely selectable between a few Hz to several kHz depending on the capacitance of the MTJ and is used as reference frequency for the lock-in amplifier, which is connected to the sample contacts. Usually, in this work, a frequency of 177 Hz is used.

Furthermore, the position of the sample is controlled by step motors in x, y and z direction with a precision of ±100 nm. The x- and y-direction correspond to moving the sample in the plane, the z-direction moves the sample in the direction of the laser beam, thus changing the beam spot size. Visual feedback is given by a camera through a confocal microscope, which is used to determine the exact position of the beam on the sample. If the MTJ position corresponds to the laser position, the magnetic field is swept, similar to the TMR measurement. With the measured Seebeck voltages in the parallel and antiparallel state and the temperature difference generated by the laser heating, the Seebeck coefficient for each orientation is calculated ($S_{p,ap} = -V_{p,ap} \cdot \Delta T$). In general, the measured thermovoltages and deduced TMS ratios are subject to a measurement error of $< 0.2\,\%$.

5.2. Determination of the beam waist

An important parameter during TMS experiments and COMSOL simulations is the size of the laser spot. It is possible to calculate the beam waist radius ω_0 with the knife edge method using a photo diode (EOT ET-2030), which records the reflected light close to a sharp edge [87, 88]. For this measurement, the beam is moved from a gold bond pad to the insulator (≅ sharp edge) while the photo diode records the intensity. The change across the edge can be expressed by

$$P_0(x) = \frac{P_{\max}}{2}\left[1 - \operatorname{erf}\left(\frac{\sqrt{2}(x - x_0)}{\omega_0}\right)\right]. \tag{5.1}$$

Here, $P_{\max}$ is the maximum diode signal, x is the position of the beam, x_0 is the position of the edge, ω_0 is the beam waist and erf is the error function. Figure 5.2 shows one beam waist measurement with two sharp

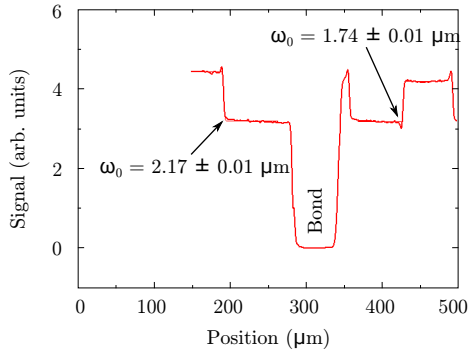

Figure 5.2.: Diode signal in dependence of the laser position on the sample in one direction. Several transitions from bond pad to insulator are observed, which are used for the extraction of the beam waist.

edges and the fits corresponding to Eq. (5.1). Since the result of the fit depends on the quality of the patterned edge, the beam waist varies slightly if different edges are probed.

By averaging over all TMS measurements and samples, a mean beam waist of $\omega_0 = (1.92 \pm 0.01)\,\mu$m is obtained when the laser is focused onto the MTJ. All COMSOL simulations use this result of the focused beam waist and, in contrast to previous works, all TMS measurements are performed with the laser focused onto the MTJ [12, 32].

The dependence of the absolute Seebeck voltage on the z-position (i.e. changing the beam waist) of the sample is depicted in Fig. 5.3(a) for three MTJ areas. Here, a z-position of $z = 0\,\mu$m corresponds to the focus of the laser beam. Although the MTJ with an area of $6\pi\,\mu\text{m}^2$ is about six times larger than the beam spot, the highest absolute Seebeck voltage is measured when the laser is focused onto the MTJ. Thus, ahead of each TMS measurement, the z-position of the sample is changed to maximize the output signal and, moreover, the generated thermovoltage.

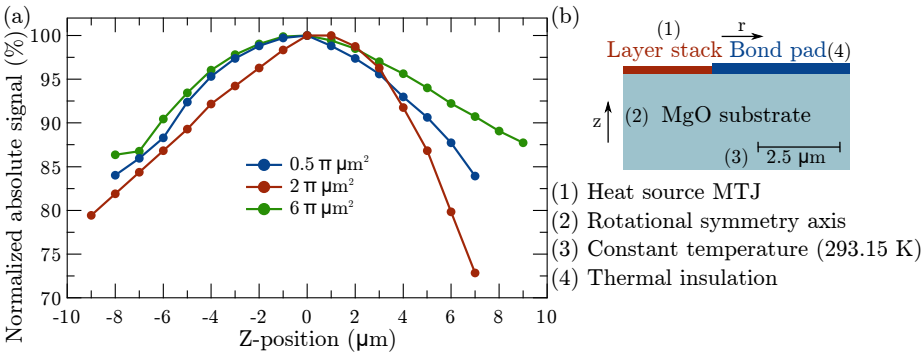

Figure 5.3.: (a) Normalized absolute Seebeck voltages for different MTJ areas and z-positions. (b) COMSOL model of the layer stack, bond pad and substrate with the necessary boundary conditions for the simulation.

5.3. COMSOL simulations

The temperature difference across the film stack and the thermal distribution across the sample, which is generated by the laser heating, is simulated with COMSOL multiphysics. This software, based on the finite element method, allows the implementation of several modules at once depending on the needs of the simulator. For this work, the module heat transfer in solids is used. To minimize computational time, a 2D rotationally symmetric model according to Fig. 5.3(b) is created, which is based on the work of Marvin Walter [12]. The heating of the laser beam is applied via a heat source on top of the MTJ, which is expressed by

$$\frac{1-R_{\mathrm{Au}}}{\lambda_{\mathrm{Au}}} \cdot \exp\left(\frac{z}{\lambda_{\mathrm{Au}}}\right) \cdot \frac{2P}{\pi\omega_0^2} \cdot \exp\left(\frac{-2r^2}{\omega_0^2}\right). \tag{5.2}$$

Here, $R_{\mathrm{Au}} = 0.591$ and $\lambda_{\mathrm{Au}} = 20\,\mathrm{nm}$ are the reflectivity and the optical penetration depth of Au at a wavelength of 637 nm, respectively. These values are adopted from Ref. [12] and kept constant during the simulations. As seen in Fig. 5.3(b), r and z describe the polar coordinates of the chosen geometry. P is the laser power, which reaches the

sample after passing through the optics. This quantity is measured with a slide power sensor from Thorlabs (Model S170C) directly in front of the sample. During different measurement periods, the relative deviation of P amounted to less than 3 mW in the course of this work. Lastly, ω_0 is the beam waist as deduced from the procedure described in Sec. 5.2.

Thermal conductivity of thin films

With this model, several simulation parameters such as the MTJ size, the laser power or the heating position can be varied. Another crucial value for the simulations is the thermal conductivity κ_t of the thin insulating barrier. In case of sputtered MgO, a thermal conductivity differing by a factor of 10 compared to the bulk value ($\kappa_{\mathrm{t,MgO}} = 4\,\frac{\mathrm{W}}{\mathrm{K\cdot m}}$ vs. $\kappa_{\mathrm{b,MgO}} = 48\,\frac{\mathrm{W}}{\mathrm{K\cdot m}}$) was found for grain sizes between 3 nm and 7 nm [89, 90]. A corresponding measurement for thin MAO films is lacking, which is why the best estimate of the thermal conductivity of thin MAO films is used in this work.

Based on the bulk value of $\kappa_{\mathrm{b,MAO}} = 23\,\frac{\mathrm{W}}{\mathrm{K\cdot m}}$ [90–92] and the factor found for MgO, a thermal conductivity of $2.3\,\frac{\mathrm{W}}{\mathrm{K\cdot m}}$ is assumed for thin MAO films. Following the discussion in Ref. [93], which finds the thermal conductivity of thin insulating films to be very sensitive to the phonon and electron temperature imbalance close to nano-magnetic interfaces, the actual thermal conductivity of the barrier might be an order of magnitude below the values used in previous publications [12, 41, 43]. During the course of this work, Kimling et al. [94] conducted first investigations of the thermal conductivity of tunnel barriers with magnetooptic Kerr effect (MOKE) thermometry experiments. They found a value of $0.9\,\frac{\mathrm{W}}{\mathrm{K\cdot m}}$ for a 2 nm MgO barrier. This results suggest that the thermal conductivity of thin films is indeed well below the value used in previous experiments. Therefore, the value of the thermal conductivity of thin MAO is assumed to be in the range of (0.2 to 2.3) $\frac{\mathrm{W}}{\mathrm{K\cdot m}}$ and (0.4 to 4) $\frac{\mathrm{W}}{\mathrm{K\cdot m}}$ in case of MgO.

In addition to the thermal conductivity, the density ρ and the heat capacity C_p of each material is needed for the simulations. Table 5.1 summarizes the material parameters used for the COMSOL simulations.

Table 5.1.: Thermal conductivity κ, density ρ and heat capacity C_p values used for the COMSOL simulations. If not stated otherwise, the values are taken from Ref. [12]. Numbers in round brackets are bulk values.

Material	$\kappa\left(\frac{\mathrm{W}}{\mathrm{K{\cdot}m}}\right)$	$\rho\left(\frac{\mathrm{kg}}{\mathrm{m^3}}\right)$	$C_p\left(\frac{\mathrm{J}}{\mathrm{K\ kg}}\right)$
Ta	57	16650	140
Ta_2O_5[a,b]	0.2	8270	306
Au	320	19320	128
Ru	117	12370	238
MnIr[c]	6	10181	316
CoFeB	87	8216	440
MAO[d,e,f]	2.3 (22-24)	3650	815
MgO	4 (48)	3580	935

[a]Ref. [95]. [b]Ref. [96]. [c]Ref. [97].
[d]Ref. [90]. [e]Ref. [91]. [f]Ref. [92].

5.4. Analysis of I/V curves

The Brinkman model [28] and the model of the intrinsic TMS [52,53] offer two different approaches to analyze I/V curves of MAO based MTJs. A detailed theoretical description is found in Sec. 2.3.2 and Sec. 3.4, respectively. Since MgO MTJs generally show a Δ_1 symmetry filter effect and, thus, exhibit coherent tunneling, the Brinkman model is not applicable. Accordingly, the analysis of I/V curves to compare between the Brinkman and the intrinsic TMS model is done for MAO MTJs only. In addition, it is possible to compare the Brinkman parameters of different samples with MAO barriers.

Brinkman model

The current density J is calculated from the measured current I and the area A of the MTJ ($J = I/A$). According to the Brinkman model, a second order polynomial fit to the differential conductance $\mathrm{d}J/\mathrm{d}V$ yields values for A, B and C, which are plugged into Eqs. 2.8 to extract the

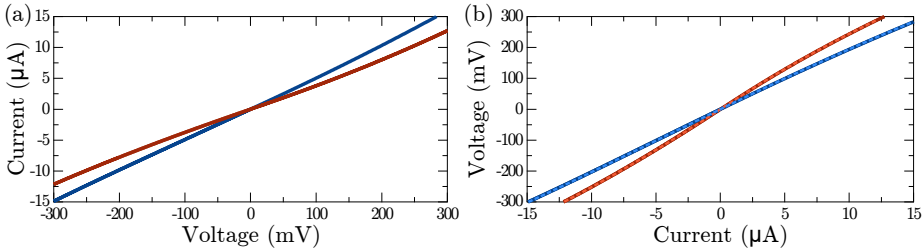

Figure 5.4.: (a) Measured I/V curve of an MTJ with 1.8 nm MAO barrier in the parallel (blue) and antiparallel (red) state. (b) Measured V/I curve of the same MTJ in the parallel (dark blue) and antiparallel (dark red) state. The dashed curves in light blue and light red depict the result of the interpolation procedure done with the measured I/V curve shown in Fig 5.4(a) and are directly on top of the measured curves.

barrier parameters φ, d_B and $\Delta\varphi$. Additionally, the effective electron mass m_eff of MAO is set to $0.422\,m_\mathrm{e}$ [98]. With A, B and C and Eq. (2.7) it is also possible to recalculate the current density depending on the voltage of the fitted Brinkman curve.

Intrinsic TMS

According to Eq. (3.11), the measurement of a V/I curve and a subsequent symmetry analysis make the extraction of the Seebeck coefficient of an MTJ possible without any external heating sources. In general, with the setups in Bielefeld and Greifswald, which are used to characterize MTJs, a voltage is applied and the resulting current is measured. Thus, an I/V curve is obtained. In order to follow the model of the intrinsic TMS, the I/V curve has to be converted to a V/I curve, which is done by an interpolation program with MATLAB. The details can be found in the Appendix V.

In order to verify the validity of this procedure, an I/V and a V/I curve are measured at the same MTJ (see Figs. 5.4(a,b)). The calculated V/I curve in comparison to the measured one is shown in Fig. 5.4(b). No difference is observed.

Part III.

Results & discussion

6. Tunnel magnetoresistance, magneto-Seebeck, and I/V measurements

6.1. Tunnel magnetoresistance results

Prior to the TMR measurements, the RA products of both series mentioned in Tab. 4.1 are measured to check the functionality of the tunneling barrier. Figure 6.1(a) sums up the RA products of the MTJs with different nominal MAO and MgO thicknesses. Here, as expected, both series show an exponential increase of the RA product in dependence of the nominal barrier thickness. Please note, that the RA products of the two MAO samples that were prepared independently agree very well with the rest of the series. In addition, both barrier materials show comparable RA products and cover six to seven orders of magnitude, providing a solid basis to study the TMR and TMS effect in dependence of the barrier thickness.

The corresponding TMR ratios, calculated with Eq. (2.1), depending on the RA products are displayed in Fig. 6.1(b). Both series show a maximum TMR ratio around a nominal barrier thickness of 2.0 nm, as predicted by theoretical calculations [57]. MTJs with MAO barrier exhibit a maximum TMR ratio of $(32 \pm 1)\,\%$, while MgO MTJs show a maximum TMR ratio of $(151 \pm 7)\,\%$. This high TMR ratio in case of MgO barriers is a direct consequence of the coherent tunneling process taking place in these MTJs. Although the maximum TMR ratios of the MTJs with MAO barrier fall short in comparison to the results of the MTJs with MgO barrier, they are still in good agreement with previous studies that used sputtering from a composite target [85]. Additionally,

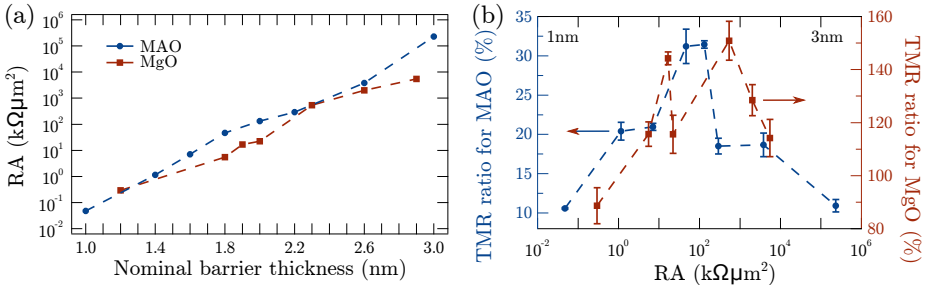

Figure 6.1.: (a) RA products of MTJs with different MAO (blue circles) and MgO (red squares) nominal barrier thicknesses. More than five elements are measured and the results are averaged. The resulting error is too small to be seen in this plot. (b) TMR ratios of MTJs with MAO (blue circles) and MgO (red squares) barrier depending on the the RA product. The error results from measuring different MTJ areas.

this relatively low TMR ratio points to a non-coherent tunneling process. Thus, the Brinkman model is applicable to MTJs with MAO barriers.

The MTJs with MgO barrier exhibit a second peak of the TMR ratio, which is directly related to the slightly increased RA product in this region. In addition, both barrier materials show a decreasing TMR ratio in the regime of very thin ($\approx 1\,\mathrm{nm}$) as well as very thick ($\approx 3\,\mathrm{nm}$) barrier thicknesses. On the one hand, the decrease in case of thin barriers is attributed to more states without Δ_1 symmetry contributing to the net tunneling current, effectively reducing the overall spin polarization and, thus, reducing the TMR ratio [26]. On the other hand, the impurity density is greatly increased for a thick barrier and, hence, the electrons lose their symmetry during the tunneling process, which also results in a lowered TMR ratio.

6.2. Tunnel magneto-Seebeck results

Since the TMS effect has not been studied with MAO barriers prior to this work, the following part deals with basic properties of the TMS effect

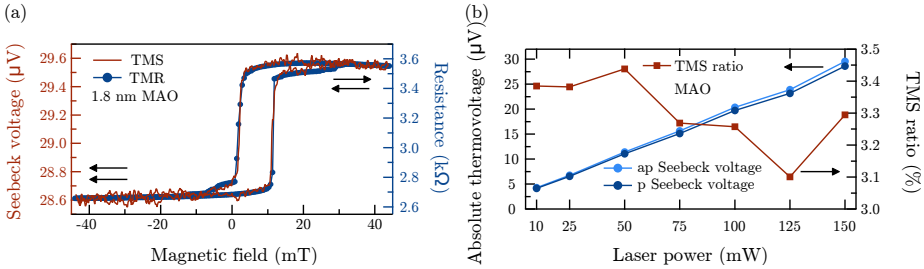

Figure 6.2.: (a) Minor TMS (red) and TMR (blue) loop of an MTJ with a nominal barrier thickness of 1.8 nm and an area of $6\,\pi\mu\mathrm{m}^2$. The black arrows indicate the parallel and antiparallel state, respectively. (b) Power dependence of the absolute thermovoltages across the whole stack and the corresponding TMS ratio.

already established for MgO based MTJs. This comparison focuses on the laser power dependence, the position dependence and the general TMS ratio of the sample with a nominal barrier thickness of 1.8 nm.

6.2.1. Tunnel magneto-Seebeck effect in magnetic tunnel junctions with $MgAl_2O_4$ barrier

Figure 6.2(a) shows a typical TMS and TMR minor loop. Clear parallel and antiparallel states are observed, which allow the extraction of the resistances $R_{\mathrm{p,ap}}$ and the Seebeck voltages $V_{\mathrm{p,ap}}$ in order to calculate the TMR ratio according to Eq. (2.1) and the TMS ratio according to Eq. (3.5). For these calculations, 20 data points in the vicinity of the maximum magnetic fields are averaged to further reduce the influence of the general measurement uncertainties. Both the TMR and the TMS effect exhibit the same switching behavior. Averaged over all elements, the TMS ratio is $(3.3 \pm 0.2)\,\%$, which is in very good agreement with comparable MgO based MTJs (TMS ratio of 2.6 %) [41].

In addition, Fig. 6.2(b) displays the dependence of the absolute thermovoltages on the applied laser power and the resulting TMS ratios. The thermovoltages increase linearly while the TMS ratio stays constant at

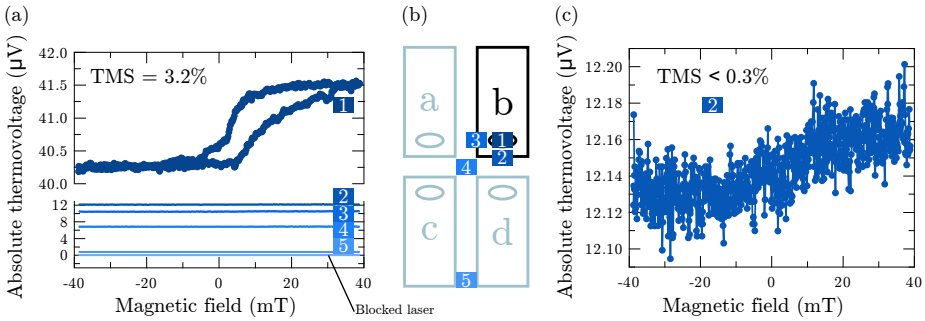

Figure 6.3.: (a) Position dependence of the thermovoltage of an MAO based MTJ with a barrier thickness of 1.8 nm. Additionally, a thermovoltage measurement with blocked laser is shown. (b) Different measurement positions on the sample with position 1 corresponding to the top of the MTJ. (c) Thermovoltage measured at position 2.

around $(3.3 \pm 0.2)\,\%$. This linear dependency is found for MgO based MTJs as well, both with the laser-induced [32, 86] and the extrinsic heating method [13, 45, 46]. Similar to the first TMS study of Walter et al. [12], a larger thermovoltage is generated in the antiparallel than in the parallel magnetic state.

Based on the final sample structure shown in Fig. 4.1(b), the laser is focused to 5 different positions close to the MTJ and some tens of μm away. The resulting TMS loops are summarized in Fig. 6.3(a). Here, position 1 corresponds to the top of the MTJ, while position 2 and 3 are on the bond pad edges in the vertical and horizontal plane, respectively. Position 4 is in the middle of the whole structure and position 5 is several tens of μm away from the MTJ. The distribution of the different positions is illustrated in Fig. 6.3(b).

Figure 6.3(c) features the TMS loop measured at position 2 on an enlarged scale. In this case, the distance to the MTJ is about 10 μm. The measured thermovoltage at this position dropped to $\approx 30\,\%$ of the thermovoltage measured with the laser focused directly on top of the MTJ. Furthermore, a TMS ratio below 0.5 % can be extracted, although almost no switching of the ferromagnetic electrodes is observable anymore.

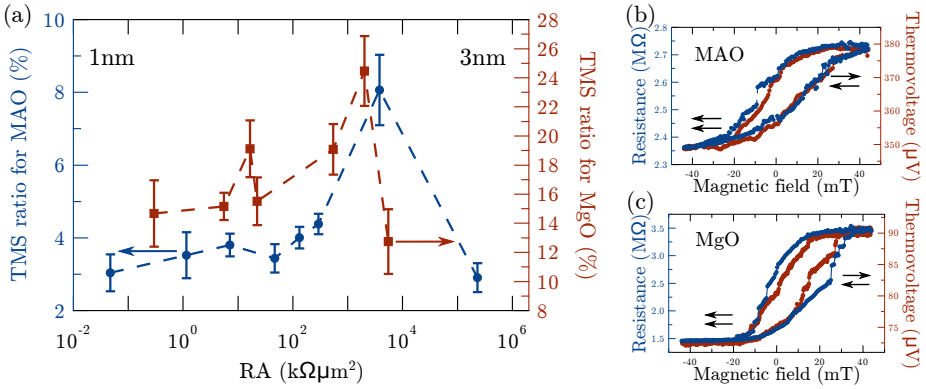

Figure 6.4.: (a) TMS ratio depending on the RA product of MAO (blue circles) and MgO (red squares) based MTJs. (b) Minor loop of a $0.5\pi\,\mu\mathrm{m}^2$ element with a nominal MAO barrier thickness of 2.6 nm. (c) Minor loop of a $0.5\pi\,\mu\mathrm{m}^2$ element with a nominal MgO barrier thickness of 2.6 nm.

With the laser focused to a position away from the MTJ, lateral heat flows emerge, which may lead to, e.g., parasitic Nernst effects. Reference [99] studies the influence of lateral heat flows in more detail.

Overall, the TMS results of an MTJ with MAO barrier are in excellent agreement with the results of preceding MgO based studies. Therefore, MAO offers vast opportunities to study the TMS effect, for example, in dependence of the barrier material and its quality. In the following section, the barrier thickness dependence of the TMS ratio of both MAO and MgO based MTJs is examined.

6.2.2. $MgAl_2O_4$ and MgO thickness variation

Similar to the TMR ratio depending on the RA product in Fig. 6.1(b), Fig. 6.4(a) depicts the dependence of the TMS ratio on the RA product of both MAO and MgO based MTJs. For this figure, all measured elements are averaged, again.

In case of thin MAO barriers, the TMS ratio increases gradually from about 3 % to 4 %. It is noteworthy, that the results of the independently

prepared samples agree very well with the rest of the series. At a nominal MAO barrier thickness of 2.6 nm, the TMS ratio shoots up to a distinct maximum of more than 8 % (see Fig. 6.4(b)) while it drops to 3 % again for a thicker barrier. MgO based MTJs reveal a very similar dependence of the TMS ratio with a distinct maximum at a nominal barrier thickness of 2.6 nm (see. Fig. 6.4(c)). Here, the TMS ratio doubles from 14 % for thin barriers to almost 28 %. Moreover, a thick barrier of MgO results in almost the same TMS ratio as thin barriers.

Both maximums are located around the same value of RA of some $10^3\,\mathrm{k\Omega\mu m^2}$ and do not coincide with the positions of the maximum TMR ratios. Usually, a direct correlation between the TMS and TMR ratio is not expected. In addition to the high TMS ratio, the MTJs with MAO barrier exhibit very high thermovoltages of more than $350\,\mu$V (cf. Fig. 6.4(b)). Up to now, the highest thermovoltages reported for CoFeB MTJs are on the order of some tens of μV [13, 45]. In Ref. [41] a sample with exchange biased CoFeB and an MgO barrier thickness of 1.5 nm is investigated, which is very similar to the MgO MTJ structure used in the work at hand.

However, a TMS ratio of only 2.6 % and a very small thermovoltage of around $3\,\mu$V is measured in this case. This huge deviation can be explained by the usage of large MTJ areas ($6\pi\mu\mathrm{m}^2$) and a defocused laser in contrast to small MTJs ($0.5\pi\mu\mathrm{m}^2$) and a focused laser beam. The effects of a defocused laser beam on the thermovoltages and the resulting TMS ratio is investigated in more detail in Ref. [99]. Before Sec. 8 deals with the thermovoltages in more detail, the I/V curves of both MAO and MgO based MTJs are discussed in the next section.

6.3. I/V curves

The corresponding I/V curves of the MTJs presented in Figs. 6.4(b,c) are shown in Fig. 6.5. Here, the raw data is already recalculated to dJ/dV curves (cf. Sec. 5.4) in order to apply the model of Brinkman to the MTJs with MAO barrier. Accordingly, a second order polynomial fit is added in case of the MTJs with MAO barrier. The fit parameters A,B

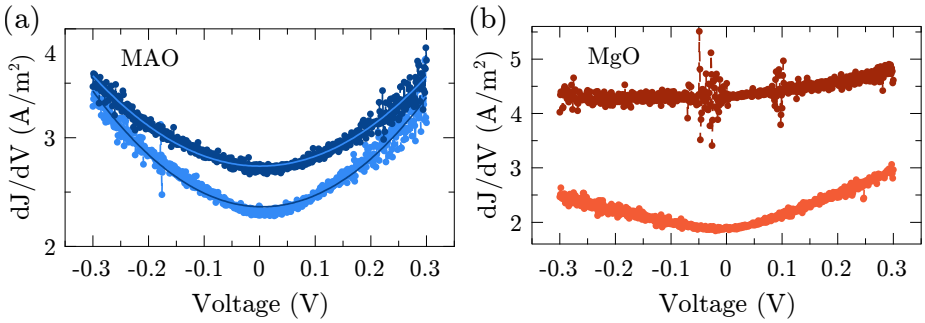

Figure 6.5.: (a) Recalculated dJ/dV curves and Brinkman fits of the MTJ with MAO barrier. (b) dJ/dV curves of the MTJ with MgO barrier. In both cases, dark color represents the parallel and light color the antiparallel magnetic state. The relatively high noise in the dJ/dV curves is related to the high resistance of several MΩs.

and C are used to extract the barrier height φ, the barrier asymmetry $\Delta\varphi$ and the barrier thickness d via Eq. (2.8).

Clearly, the dJ/dV curves of the MgO MTJ show a different behavior than the dJ/dV curves of the MAO MTJ. While the parallel curve is almost constant, i.e. the I/V curve is linear, the antiparallel curve shows a nearly rectangular kink at a bias voltage of $V = 0\,\mathrm{mV}$. These curve shapes are typical for MgO based MTJs and reflect the influences of the coherent tunneling processes. In contrast, both dJ/dV curves of the MTJ with MAO barrier show the same quadratic characteristics. The differences between the dJ/dV curves of the MTJs with MAO and MgO barrier illustrate once again, why the Brinkman model is used for MAO based MTJs only.

6.4. Brinkman parameters

Figure 6.6 sums up the Brinkman parameters extracted from all measured I/V curves. In Fig. 6.6(a), the Brinkman barrier thickness d_B is compared to the nominal barrier thickness d_N.

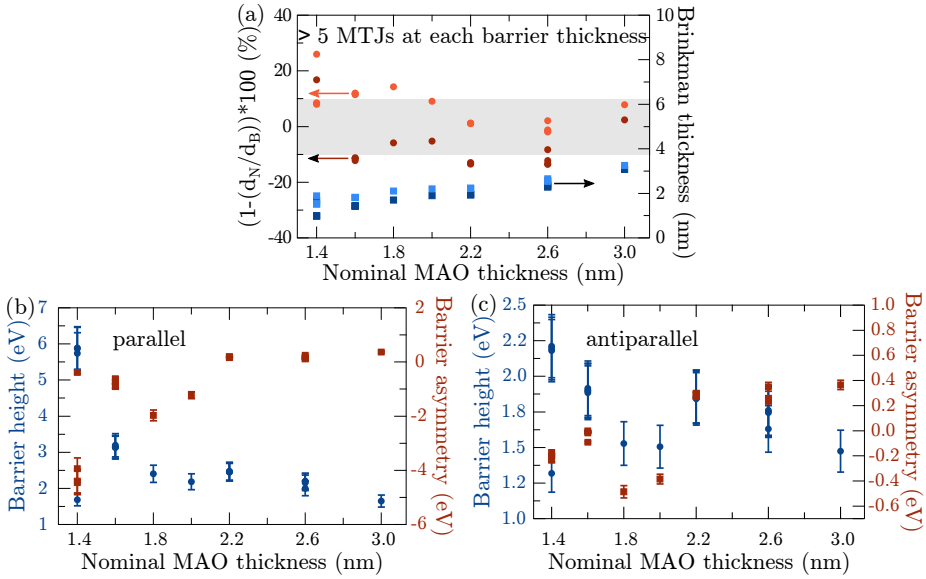

Figure 6.6.: (a) Brinkman barrier thickness d_B (blue) depending on the nominal barrier MAO thickness d_N with relative deviation between the two (red) in percent. Light colors are antiparallel, dark colors parallel magnetization orientation. The gray area is the standard error of 10 % assumed by the Brinkman model. (b,c) Barrier height φ and barrier asymmetry $\Delta\varphi$ depending on the nominal barrier thickness for parallel and antiparallel state, respectively.

The gray area represents the standard error of 10 % assumed by the Brinkman model. Since most of the elements show a deviation that is close to or less than 10 %, the real barrier thickness is close to the nominal one. Additionally, measurements performed in the antiparallel state generally result in higher values than the parallel counterpart. Again, the samples prepared independently agree very well with the results of the rest of the series. The only statistical outlier is caused by the sample with a thin MAO barrier of 1.4 nm, which can be explained by the requirement of the Brinkman model that the barrier thickness must be larger than 10 Å. As 1.4 nm is close to this condition, the extracted val-

ues cover a wide spectrum. This effect is also observed for the barrier height and the barrier asymmetry (cf. Figs. 6.6(b,c)). Thus, the sample with a barrier of 1.4 nm is not taken into account for further analysis.

In case of the barrier height, pictured in Fig. 6.6(b) for the parallel magnetization alignment and in Fig. 6.6(c) for the antiparallel magnetization alignment, consistent results are obtained between the samples that were independently prepared. With increasing barrier thickness, the barrier height decreases gradually from over 3 eV to 1.7 eV in the parallel and from 1.9 eV to 1.5 eV in the antiparallel state. Additionally, the barrier asymmetry increases from -1 eV to 0.5 eV in the parallel state and from -0.1 eV to 0.4 eV in the antiparallel state. However, the separately deposited samples show a deviation from the general trend observed for the rest of the series. A reason for this deviation might be the deposition process itself, which plays a vital role for the final barrier asymmetry.

Nevertheless, the obtained Brinkman parameters offer valuable insight regarding a qualitative comparison of MAO based MTJs with varying barrier thickness. In the next section, an I/V curve of the sample with the highest TMR ratio is analyzed in more detail, particularly with regard to the method of the intrinsic TMS.

6.5. Comparison of laser-induced and intrinsic TMS

The sample with the highest TMR ratio exhibits the largest differences with regard to the parallel and antiparallel I/V curve at the same time. Thus, the symmetry analysis of the intrinsic model in comparison to the results of the laser-induced TMS is most suited for this sample. With regard to the model (see Sec. 3.4) and the experimental procedure (see Sec. 5.4 and Appendix V), Figs. 6.7(b,c) display the antisymmetric and symmetric parts of the V/I curve of an MTJ with a barrier of 1.8 nm MAO. In addition, the Brinkman fits and resulting Brinkman parameters of the corresponding MTJ are shown in Fig. 6.7(a).

The antisymmetric part of the V/I curve (Fig. 6.7(b)) reveals a deviation from the expected linear behavior for currents above 60 μA in both magnetic states. This deviation is caused by the change of the resistance

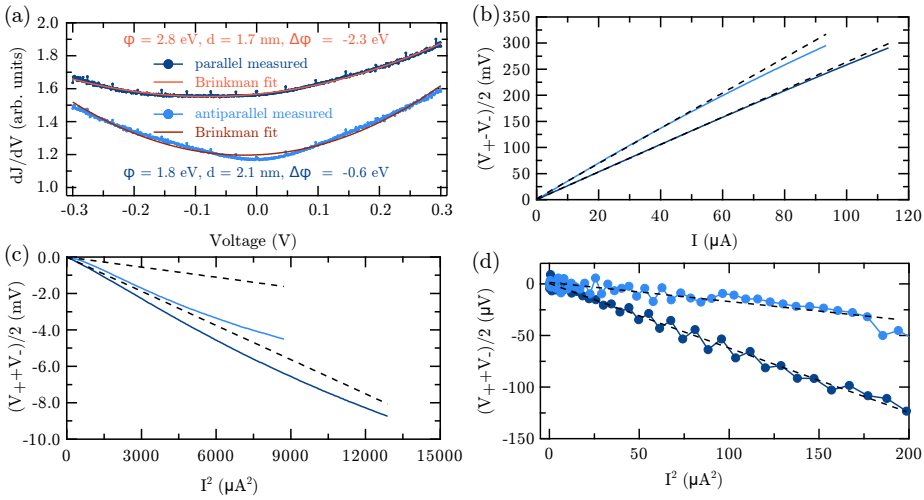

Figure 6.7.: (a) dJ/dV curves of an MTJ with a barrier of 1.8 nm MAO with corresponding Brinkman fits and parameters. (b) Antisymmetric part of the V/I curve. (c) Symmetric part of the V/I curve. (d) Enlarged section of the symmetric part shown in (c). Light blue represents the antiparallel state, dark blue the parallel state and black dashed lines are linear fits.

of the junction due to the increased base temperature in case of higher currents. In the symmetric part, this deviation gets even more prominent (Fig. 6.7(c)), which is why an enlarged section of the symmetric part is used to perform a linear fit in accordance with the intrinsic TMS model (see Fig. 6.7(d)). The linear fit is then extended to the whole range. Clearly, the linear fits in the parallel and antiparallel state are not able to explain the observed symmetry features.

As a direct comparison, Fig. 6.8 depicts the results of the symmetry analysis of an MTJ with an MgO barrier thickness of 2.0 nm. Again, the antisymmetric contribution of the antiparallel state deviates from a linear behavior (see Fig. 6.8(b)). However, the parallel antisymmetric contribution increases linearly, even for higher currents. In contrast, the parallel symmetric contribution shows a non-linear contribution, result-

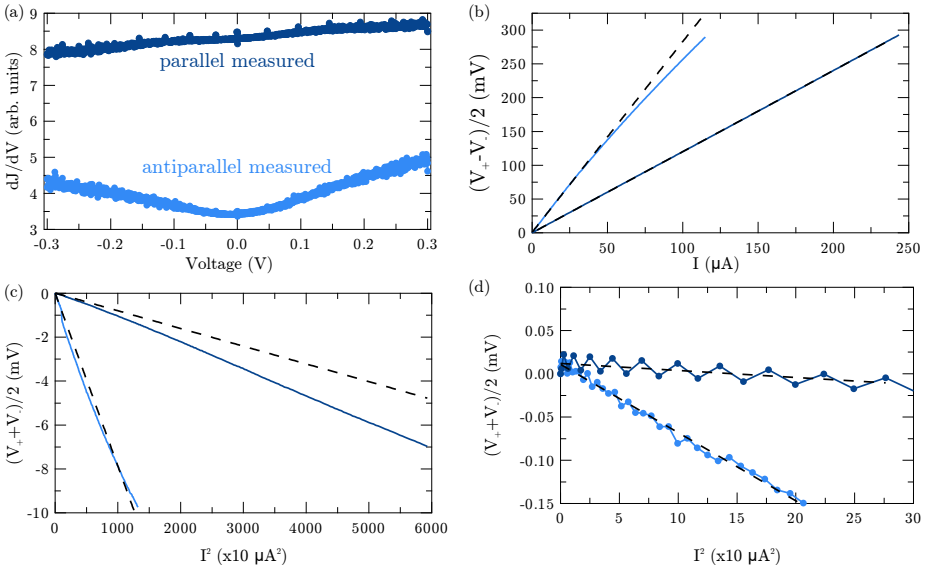

Figure 6.8.: (a) dJ/dV curves of an MTJ with a barrier of 1.8 nm MgO. (b) Antisymmetric part of the V/I curve. (c) Symmetric part of the V/I curve. (d) Enlarged section of the symmetric part shown in (c). Light blue represents the antiparallel state, dark blue the parallel state and black dashed lines are linear fits.

ing in a clear deviation from the linear behavior, while the antiparallel symmetric part is sufficiently approximated by a linear fit (Fig. 6.8(c)). The linear fits are done in the enlarged section seen in Fig. 6.8(d).

For both MAO and MgO, the symmetry analysis reveals deviations from the expected linear behavior. Nevertheless, the extraction of the slopes of the symmetric parts allows an approximate calculation of the Seebeck coefficients within the intrinsic TMS model. In order to follow this model, the thermal asymmetric parameter $\alpha = \sum(\eta_j R_{\kappa j} R_j)$ needs to be calculated. Since the resistance of both MTJs is mostly governed by the barriers ($\approx$ kΩ vs. $\approx \Omega$), the influence of the other layers can be excluded in a first approximation and

$$\alpha = \sum(\eta_{\mathrm{j}} R_{\kappa\mathrm{j}} R_{\mathrm{j}}) \tag{6.1}$$

simplifies to

$$\alpha \approx \eta_{\mathrm{MAO/MgO}} R_{\kappa} R. \tag{6.2}$$

Here,

$$\eta_{\mathrm{MAO/MgO}} = \frac{\Delta \mathrm{T} \kappa \sigma}{J^2 d^2}, \tag{6.3}$$

with the temperature gradient ∇T, the thermal and electrical conductivity κ and σ (which are also depending on the barrier material), the current density J and the barrier thickness d. Except for the temperature gradient and the thermal conductivity, all parameters are known for both MAO and MgO. Following the discussion about the thermal conductivity of thin films in Sec. 5.3, a thermal conductivity of 2.3 $\frac{\mathrm{W}}{\mathrm{K\,m}}$ (4 $\frac{\mathrm{W}}{\mathrm{K\,m}}$) is assumed for MAO (MgO). Additionally, with a mean current of 50 μA for the MAO based MTJ (taken as an average from the I/V curves) and a mean current of 100 μA for the MgO based MTJ, the temperature gradient is assumed to be 25 $\frac{\mathrm{mK}}{\mathrm{nm}}$ in case of MAO and 50 $\frac{\mathrm{mK}}{\mathrm{nm}}$ in case of MgO. In comparison, Zhang, Teixeira et al. [52, 53] assumed a temperature gradient of $75 - 195$ $\frac{\mathrm{mK}}{\mathrm{nm}}$ generated by a current of 0.4 mA. Hence, the temperature gradient assumption for the MAO and MgO MTJ represents the upper limit.

The resulting values of the intrinsic TMS model are summarized in Tab. 6.1. Here, the antisymmetric slopes (asym.) yield values for the resistance of the MTJ that are in good agreement with the resistances R deduced from TMR loops. In the antiparallel state, the extracted slope of the antisymmetric contribution shows a larger deviation from the measured resistance than in the parallel state for both MTJs. This difference is attributed to the deviation of the antisymmetric contribution from the linear behavior. In general, the error of the fits to the antisymmetric and symmetric contribution are very small due to the fit procedure in the enlarged section.

Table 6.1.: Results of the intrinsic symmetry evaluation. Asym./sym. corresponds to the antisymmetric/symmetric slope. As a direct comparison, the resistances R as deduced from TMR loops are given.

MTJ [state]	asym. (kΩ)	R (kΩ)	sym. (V/A^2)	α (K/A^2)
MAO [p]	2.6 ± 0.1	2.7 ± 0.1	$-6.3 \cdot 10^{11} \pm 10^{10}$	$5.4 \cdot 10^5$
MAO [ap]	3.4 ± 0.1	3.6 ± 0.1	$-1.8 \cdot 10^{11} \pm 10^{10}$	$5.4 \cdot 10^5$
MgO [p]	1.2 ± 0.1	1.2 ± 0.1	$-8.1 \cdot 10^{13} \pm 10^{12}$	$5.9 \cdot 10^4$
MgO [ap]	2.8 ± 0.1	3.0 ± 0.1	$-7.9 \cdot 10^{14} \pm 10^{13}$	$5.3 \cdot 10^4$

According to the intrinsic TMS model, it is possible to calculate the Seebeck coefficients of the MTJs via $S = \text{slope}/\alpha$. Table 6.2 sums up the results of the intrinsic TMS as well as the results of the laser-induced TMS for the MTJs with a 1.8 nm MAO and a 2.0 nm MgO barrier. The errors of the laser-induced Seebeck coefficients originate from the uncertainty of the temperature difference across the barrier as discussed in Sec. 7, while the error of the TMS ratio stems from the measured thermovoltages.

Overall, results obtained with the intrinsic model do not agree with the laser-induced results. In case of the MAO MTJ, the absolute parallel Seebeck coefficient is larger than in the antiparallel case, which leads to a negative TMS ratio. This result directly contradicts the Seebeck coefficients and TMS ratio measured with the laser-induced TMS. In addition, the symmetry analysis yields very high Seebeck coefficients ($> 10000\,\mu$V/K) in case of the MgO based MTJ in the antiparallel state. Here, the absolute values of the Seebeck coefficients show the opposite behavior, which is not confirmed by the laser-induced TMS experiments. All laser-induced TMS measurements exhibit a larger thermovoltage in the antiparallel than in the parallel magnetic state, independent of barrier material or barrier thickness. Moreover, the intrinsic TMS model generates large TMS ratios, which can not be confirmed by the results of the laser heating.

The Brinkman model offers an alternative way to study I/V curves

Table 6.2.: Seebeck coefficients of the intrinsic TMS model and the laser-induced TMS as a direct comparison. Details about the temperature differences to calculate the Seebeck coefficients of the laser-induced TMS are provided in Sec. 7. The errors of the laser-induced Seebeck coefficients are based on the uncertainty of the thermal conductivity of the tunnel barrier.

	$S_\mathrm{p}\ \left(\frac{\mu\mathrm{V}}{\mathrm{K}}\right)$	$S_\mathrm{ap}\ \left(\frac{\mu\mathrm{V}}{\mathrm{K}}\right)$	TMS (%)
MAO MTJ			
intrinsic	-1.2 ± 0.1	-0.3 ± 0.1	-75 ± 10
laser	-4.3 ± 1.8	-4.4 ± 1.9	3.3 ± 0.2
MgO MTJ			
intrinsic	-1370 ± 20	-14900 ± 200	91 ± 1
laser	-6.5 ± 2.5	-7.4 ± 2.8	16 ± 1

and the related symmetries of MAO based MTJs. Equation 2.7 in combination with the extracted Brinkman parameters of the MAO MTJ (cf. Fig. 6.7) allow to simulate an I/V curve. This I/V curve is subject to the same symmetry analysis as before and compared with the results of the real I/V. Figure 6.9 shows both the symmetric contribution of the simulated and the real V/I curve as well as two symmetric contributions with different barrier asymmetries.

Clearly, the barrier asymmetry of the Brinkman model plays a vital role concerning the symmetric contribution of the V/I curve. With a vanishing barrier asymmetry, i.e. a purely symmetric barrier, the symmetric contribution of the simulated V/I curve vanishes completely. Reversing the sign of the barrier asymmetry results in a reversed symmetric contribution. In principal, a reversed barrier asymmetry corresponds to reversing the current direction inside the MTJ. As a result, the Seebeck coefficient changes its sign within the model of the intrinsic TMS.

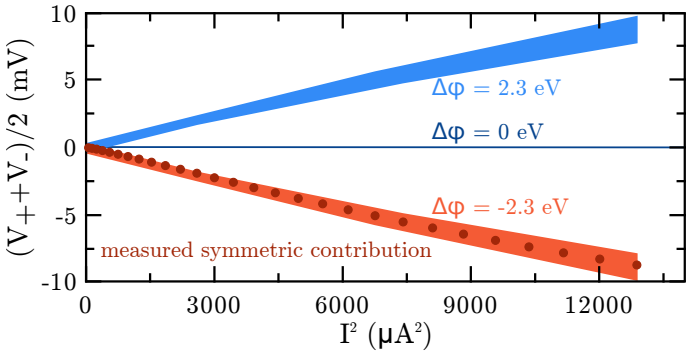

Figure 6.9.: Symmetric contributions of the V/I curve in the parallel state (dark red), the corresponding simulated V/I curve (light red), a simulated V/I curve with a vanishing barrier asymmetry (dark blue) and with a barrier asymmetry of opposite sign (light blue). The area of each simulated symmetric contribution represents the typical error range of the Brinkman model of 10 %.

In addition, the simulated symmetric contribution (within the typical error range of the Brinkman model) agrees very well with the measured symmetric contribution. Thus, without any assumptions about a temperature difference or the inclusion of Seebeck coefficients, the Brinkman model with barrier asymmetry, barrier height and barrier thickness fully explains the observed symmetric contributions of the V/I curve.

The next section deals with COMSOL simulations of the temperature differences inside an MTJ due to laser heating. They allow the calculation of Seebeck coefficients, as already used for the evaluation of the laser-induced TMS results in Tab. 6.2.

7. Determination of thermal profiles via COMSOL simulations

The following simulations are based on the model described in Sec. 5.3. As the thermal conductivity of the thin insulating barrier is the biggest unknown quantity within these simulations, its influence on the final temperature distribution is displayed in Fig. 7.1. This simulation is performed with a laser power of 120 mW that is applied to the smallest MTJ size of $0.5\pi\mu\mathrm{m}^2$.

Firstly, Fig. 7.1(a) shows the distribution of the temperature difference ΔT depending on the thermal conductivity ranging from the thin film (marked by the gray area) to the bulk regime. The resulting temperature differences for bulk MAO and bulk MgO are highlighted for two barrier thicknesses. Almost no difference between the two barrier materials is observed in this regime. Secondly, Fig. 7.1(b) depicts the thin film regime. Here, the temperature difference strongly depends on the thermal conductivity of the barrier resulting in huge differences for the two materials. For both MAO and MgO, the upper limits of the thin film thermal conductivity are marked. According to the discussion described in Sec. 5.3, the actual thermal conductivity of both MAO and MgO can be well below the highlighted values in Fig. 7.1(b). Thus, very large temperature differences across the stack of several tens of K become possible. Additionally, the extracted temperature differences and, in turn, the calculated Seebeck coefficients are afflicted with huge errors.

Hence, the simulated temperature differences should be treated with caution and can only provide a rough estimate. Previous works [12, 41, 43, 44] dealt with temperature differences of the order of several tens of mK. This deviation is due to the large spot size of hundreds of $\mu\mathrm{m}^2$ in contrast to $\approx 12\,\mu\mathrm{m}^2$ used in this work.

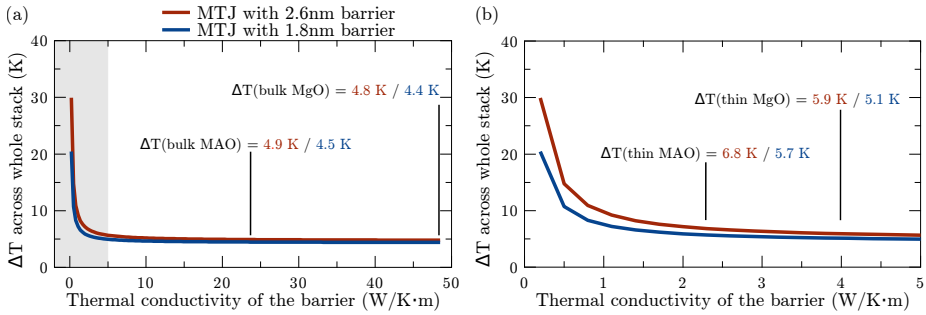

Figure 7.1.: (a) Temperature difference across the whole stack with an MTJ area of $0.5\pi\mu m^2$ and a laser power of 120 mW in dependence of the thermal conductivity of the barrier. Two barrier thicknesses and values for bulk MAO and MgO are shown. (b) Enlarged section of (a) with the assumed upper limit thin film conductivities of MAO and MgO. The density ρ and heat capacity C_p do not change the outcome of the simulation.

Figure 7.2 presents the temperature differences across an MTJ with a MAO barrier of 1.8 nm and the change of the base temperature of the top electrode in dependence of the MTJ area. Overall, the temperature differences across the barrier and the whole stack show the same linear behavior for larger MTJs. In addition to the temperature differences, the laser heating also results in an increased base temperature of the top electrode depending on the MTJ area. This finding is explainable by the larger Au pad on top of the larger MTJs effectively absorbing more heat. If the MTJ size is much larger than the laser spot, this effect saturates. In case of very small MTJs, i.e. the MTJ area is much smaller than the laser spot, the temperature differences exhibit a deviation of the aforementioned linear behavior. Here, a rapid increase of the temperature differences is observed.

The dependence of the temperature difference across the whole stack on the applied laser power is visualized in Fig. 7.2(b) for an MAO barrier thickness of 1.8 nm and an MTJ area of $0.5\,\pi\mu m^2$. A clear linear behavior is observed, which directly explains the linear behavior of the

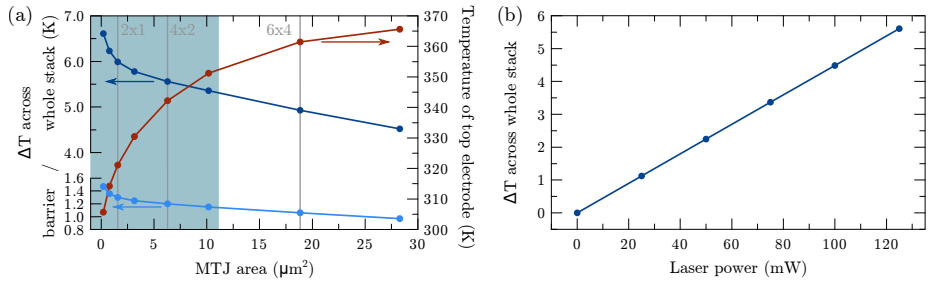

Figure 7.2.: (a) Temperature differences across barrier (bottom left scale) and the whole stack (top left scale) in dependence of the MTJ area for an MAO barrier of 1.8 nm and a laser power of 120 mW. The right scale shows the changing temperature of the top electrode. The dark gray area represents the size of the laser spot and the three experimentally realized MTJ areas are highlighted by the light gray vertical lines. (b) Dependence of the temperature difference across the whole stack on the applied laser power with an MTJ area of $0.5\,\pi\mu\mathrm{m}^2$ and a barrier thickness of 1.8 nm of MAO.

measured thermovoltages in Fig. 6.2(b) and verifies the proportionality of temperature difference and measured thermovoltage.

In Figs. 7.3(a,b), the resulting thermal distribution across the whole stack is presented for MAO barrier thicknesses ranging from 1.4 nm to 2.6 nm. Again, an MTJ size of $0.5\,\pi\mu\mathrm{m}^2$ is used for the simulation. The lower limit of the thermal conductivity ($0.3\,\frac{\mathrm{W}}{\mathrm{Km}}$) of MAO is shown in Fig. 7.3(a), while the upper limit ($2.3\,\frac{\mathrm{W}}{\mathrm{Km}}$) is shown in Fig. 7.3(b). As a result, the temperature differences across the barrier and the whole stack are summarized in Fig. 7.3(c). Here, the distance between, e.g., the dark colored lines gives an impression of the uncertainty of the final temperature difference. In this case, the error amounts to several K.

Additionally, the thermal distributions across the whole stack offer insight to other temperature differences building up. Since the metallic layers have a relatively high thermal conductivity, almost no temperature difference is observed, except for the MnIr layer. Its low thermal conductivity of $6\,\frac{\mathrm{W}}{\mathrm{Km}}$ results in a huge contribution to the overall temper-

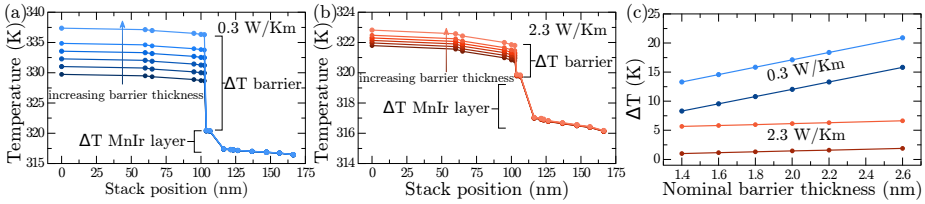

Figure 7.3.: (a,b) Temperature distribution across the whole stack for barrier thicknesses ranging from 1.4 nm to 2.6 nm. (a) The thermal conductivity of MAO is set to 0.3 $\frac{\mathrm{W}}{\mathrm{Km}}$ and (b) 2.3 $\frac{\mathrm{W}}{\mathrm{Km}}$, respectively. (c) Extracted temperature differences across the whole stack (light colors) and the barrier (dark colors) depending on the barrier thickness and the low thermal conductivity (blue) and high thermal conductivity (red).

ature difference and can even become larger than the actual temperature difference across the barrier (cf. Fig. 7.3(b)).

The influence of the beam waist on the temperature difference is pictured in Fig. 7.4(a) for an MTJ with an MAO barrier thickness of 1.8 nm and an area of 0.5 $\mu\mathrm{m}^2$. For this simulation, a laser power of 120 mW and an MAO thermal conductivity of 2.3 $\frac{\mathrm{W}}{\mathrm{Km}}$ is used. Reference [99] measures the thermovoltage depending on the beam waist and finds a behavior that agrees very well with the simulation of the temperature differences.

Both measurement and simulation exhibit a trend that is $\propto 1/\omega_0^2$. Thus, for small beam waists, i.e. focusing the laser, the temperature differences are greatly increased in comparison to, e.g., the values used in the simulations of Walter et al. [12]. Here, usual temperature differences are around several mK.

In addition to changing the laser beam waist, Fig. 7.4(b) depicts the influence of a changed heating position. For this simulation, the edge of the bond pad close to the MTJ is heated with a laser power of 120 mW. The resulting temperature distributions inside an MTJ with a 1.8 nm MAO barrier and an area of 0.5 $\mu\mathrm{m}^2$ are shown in case of heating the MTJ on top (blue) and on the edge of the bond pad (red). Clearly, the heating at the edge of the bond pad results in a reduction of the over-

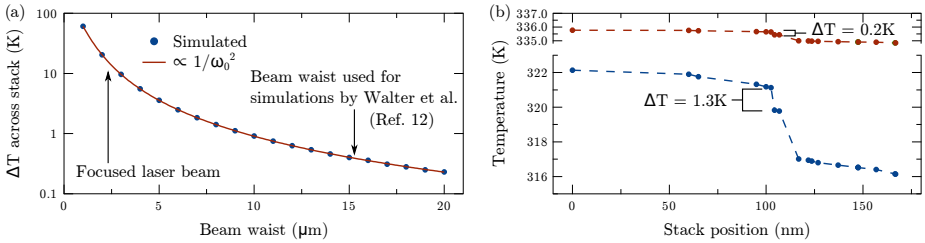

Figure 7.4.: (a) Beam waist influence on the temperature difference across the whole stack. The obtained simulation is best fitted with a function that is $\propto 1/\omega_0^2$ (please note the logarithmic scale). Both values for the different beam waists of this work (focused beam) and Ref. [12] are marked. (b) Thermal distributions for heating the MTJ directly on top (blue) and on the edge of the contact pad (red).

all temperature difference to about 15 % of the temperature difference obtained with heating the MTJ on top.

However, the base temperature is increased when heating the bond pad in contrast to heating the MTJ. This result agrees with the increased base temperature for larger MTJs as observed in Fig. 7.2. Within the simulations, using a generally increased area as heat source leads to an increased base temperature of the whole stack. So far, an influence of the base temperature of the stack on TMR or TMS measurements has not been observed experimentally. Nevertheless, a platinum thermometer as used by Krzysteczko et al. [100] close to the MTJ could provide valuable insight in the future.

With the results of the COMSOL simulations, the according temperature differences and the measured thermovoltages, the calculation of Seebeck coefficients become possible. However, based on the uncertainty regarding the thermal conductivities of the thin insulating barriers, the errors of the extracted temperature differences are in the range of several K. Thus, in general, COMSOL simulations are able to give a qualitative rather than a quantitative impression of the processes taking place inside a laser heated MTJ.

In the next section, the knowledge about the temperature distributions

inside the MTJ is used to calculate Seebeck coefficients in combination with the measured thermovoltages.

8. Thermovoltages and Seebeck coefficients

This section focuses on the thermovoltages and the resulting Seebeck coefficients of MAO and MgO based MTJs, which are calculated with the COMSOL simulation results of the previous section. Firstly, the measured thermovoltages in the parallel state depending on the RA product and the barrier material are presented in Fig. 8.1(a).

Here, in contrast to Fig. 6.4, only MTJs with an area of $6\pi\,\mu\mathrm{m}^2$ are shown, because the thermovoltages depend heavily on the MTJ area (cf. Fig. 8.1(b)). It was not possible to measure thermovoltages for every MTJ area and barrier thickness. Especially, thin MgO barriers of small MTJs proved to be very vulnerable, which might be related to the MgO roughness. The remaining MgO MTJs exhibit thermovoltages of up to $50\,\mu\mathrm{V}$ in case of thick barriers. Around a barrier thickness of 2 nm a dip of the thermovoltages is observed, which is also present for the MAO MTJs. However, the two MAO based samples showing a decreased thermovoltage are the samples, which have been prepared independently. Thus, a comparison with the absolute thermovoltages of the rest of the series appears to be problematic, since the lead contributions might change. Another important factor might be the installation of the automated sample position controller between the measurements. With this controller, the adjustment of the laser focus became more precise. As seen in Fig. 5.3, the measured thermovoltage is heavily dependent on the laser focus, i.e. the z-position.

Nevertheless, the other MAO MTJs show thermovoltages, which are generally higher in comparison to the MgO based MTJs. The MAO based sample with the doubled TMS ratio (cf. Fig. 6.4(b)) exhibits the highest thermovoltages with up to $380\,\mu\mathrm{V}$ in the antiparallel state, whereas the

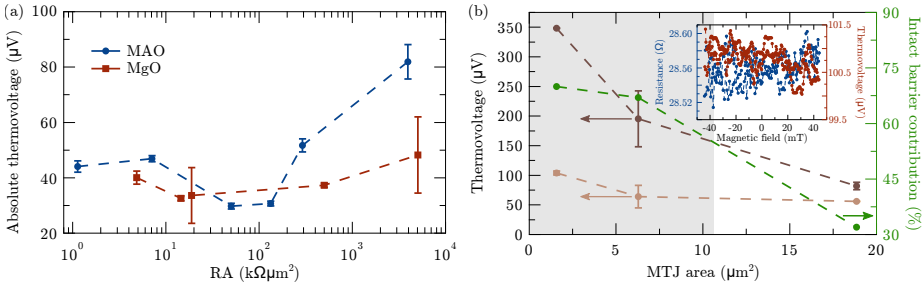

Figure 8.1.: (a) Thermovoltages measured at MAO and MgO based MTJs in the parallel state with an area of $6\pi\,\mu\mathrm{m}^2$ and a laser power of 120 mW depending on their RA product. (b) Thermovoltages with intact (dark gray) and destroyed (light gray) MAO barrier in dependence of the MTJ area. Also, the contribution of the intact barrier to the absolute thermovoltage is displayed (green) as well as the laser spot size (gray area). The inset shows the remaining resistance and thermovoltage after the dielectric breakdown of the barrier.

comparable MgO based MTJ shows thermovoltages around $90\,\mu$V (cf. Fig. 6.4(c)). Figure 8.1(b) displays the dependence of the thermovoltage on the MTJ area of the sample with MAO barrier. A nonlinear decrease of the thermovoltage with increasing MTJ area is observed, which is caused by the occurrence of non homogenous heating of the MTJs. The laser spot size is added in this picture as gray area in order to distinguish between the regime of homogenous and non homogenous heating.

Additionally, the MTJs are subject to a high voltage of $> 3\,$V after the TMS and thermovoltage measurements to dielectrically destroy the barrier (see inset of Fig. 8.1). The remaining thermovoltage provides information of the barrier contribution to the overall absolute thermovoltage. This contribution decreases rapidly from $\approx 70\,\%$ for homogeneously heated MTJs to $\approx 30\,\%$ in case of the laser spot being much smaller than the MTJ area. This effect underlines the importance of homogenous heating during laser-induced TMS measurements.

Furthermore, the absolute thermovoltage with and without the contri-

bution of the barrier allows conclusions about the individual temperature gradients. Since the contribution of an intact barrier amounts to 70 % in case of small MTJ areas, the temperature gradient of the rest of the stack is responsible for 30 % of the absolute thermovoltage. Most of this remaining temperature gradient builds up across the MnIr layer due to its low thermal conductivity. This fact is also visualized in Figs. 7.3(a,b). Thus, $V_{MAO} \approx \frac{7}{3} V_{MnIr}$, with the measured thermovoltages V in case of only MAO and MnIr contributing. Via $V = -S\Delta T$ and the fact that $\Delta T \propto \frac{1}{\kappa}$ this equation can be rewritten to $\kappa_{MAO} = \frac{3}{7}\kappa_{MnIr}$. Additionally, the different thicknesses of the layers need to be taken into account. All in all, a thermal conductivity of MAO of $\approx 0.7 \frac{W}{Km}$ is obtained with this evaluation, which is well within the limits assumed for the thermal conductivity of thin MAO films in this work.

In order to allow a direct comparison, the same evaluation is performed at the sample with the same nominal barrier thickness of 2.6 nm MgO. Moreover, the smallest, homogeneously heated MTJs are chosen again. The remaining absolute thermovoltage after a dielectric breakdown of the MgO barrier amounts to 79 % of the overall thermovoltage. Thus, a thermal conductivity of $5.8 \frac{W}{Km}$ is obtained for thin MgO barriers. This value is in the same range of the experimental value found by Lee et al. [89] for grain sizes between 3 nm and 7 nm ($4 \frac{W}{Km}$), but far away from the value proposed by theoretical predictions and recent MOKE experiments [93, 94] ($(0.4 \text{ to } 0.9) \frac{W}{Km}$).

In the following, the Seebeck coefficients of the MAO and MgO based MTJs are deduced from the measured thermovoltages and the COMSOL simulations presented in Sec. 7. Figure 8.2 summarizes the extracted Seebeck coefficients for both barrier materials and the parallel and antiparallel magnetic state, respectively. For the calculation, the upper limit of the thermal conductivity, i.e. the lower limit of the temperature difference, is used. The influence of the uncertainty of the thin film thermal conductivity is exemplarily shown for an MAO barrier thickness of 1.8 nm and an MgO barrier thickness of 1.9 nm.

While the Seebeck coefficients of the MgO based MTJs are almost constant around $(-9 \text{ to } -10)\,\mu V/K$, the Seebeck coefficients of the MAO based MTJs rise to more than $-16\,\mu V/K$ in case of thick barriers. Again,

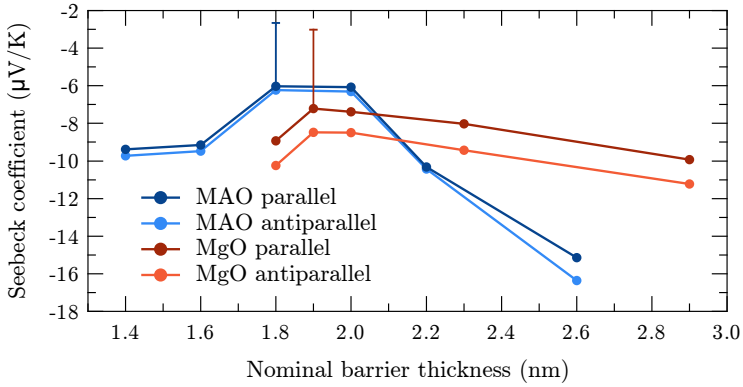

Figure 8.2.: Seebeck coefficients for MTJs with MAO and MgO barrier in dependence of the nominal barrier thickness. The height of the error is indicated for MAO and MgO.

the independently prepared samples show slightly reduced Seebeck coefficients, which is due to the aforementioned differences in the measured thermovoltages.

Although the large temperature differences lead to relatively small Seebeck coefficients, they are in good agreement with preceding studies [12, 50, 101]. In particular, Böhnert et al. [48] find an average Seebeck coefficient of $(-18 \pm 2)\,\mu$V/K in comparable MgO MTJs, which agrees very well with the values found in this work even if the uncertainty of the thermal conductivity is taken into account.

Overall, the absolute values of the Seebeck coefficients need to be treated with caution due to the large uncertainties regarding the actual temperature differences across the MTJs. A detailed investigation including for example Pt thermometer strips close to the top and the bottom of the MTJ might provide valuable insight. However, this approach greatly increases the complexity of the patterning process and the setup in general. Another approach is the determination of thermal conductivities via MOKE experiments, which yielded promising preliminary results [94].

Part IV.

Summary & Outlook

9. Summary & Outlook

In this chapter, the results obtained during this work are briefly recapped and summarized. At first, basic investigations of MTJs with an MAO barrier revealed very similar results in contrast to previous studies conducted with MgO based MTJs. For example, the same linear power dependence, a comparable position dependence and an equivalent TMS switching in comparison to the TMR switching was found. Thus, in general, MAO as a barrier material is very suitable to study laser-induced effects in MTJs.

During the course of this work, several MAO MTJs were prepared with various sputtering parameters in order to improve the TMR ratio. However, the TMR effect remained relatively low at around 30 % with barrier thicknesses of 2.0 nm. Thus, this ratio is considered the maximum possible effect achievable with the used composite target. A first shot with evaporated MAO barriers in contrast to sputtered MAO barriers revealed improved TMR and TMS results. Figure 9.1 depicts a TMR and TMS minor loop of an MTJ with an evaporated MAO barrier. The relatively low RA product of $\approx 300\Omega\mu\mathrm{m}^2$ in comparison to the other samples (cf. Fig. 6.1) suggests a thin barrier even below 1.5 nm.

In general, the thickness of the evaporated barrier is hard to control, since the deposition rate depends heavily on the position of the electron beam on the target material. Thus, this method was not applicable in this work. Nevertheless, the MTJ with evaporated MAO barrier exhibits a high TMR ratio of more than 50 % and a high TMS ratio of 15 %. As suggested by Ref. [83], the reason for the high ratios might be the decreased lattice mismatch with the ferromagnetic electrodes, which, in turn, is due to the lower energies involved during the evaporation process in comparison to sputtering of the barrier material. Overall, evaporated MAO barriers might offer a possibility to further improve and study the

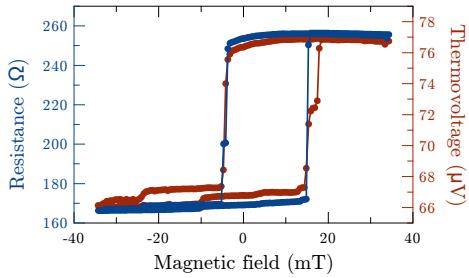

Figure 9.1.: TMR and TMS loop of an MTJ with evaporated MAO barrier. The TMR effect amounts to 53 %, while the TMS effect is 15 %.

effects of temperature differences within MTJs. Since lattice matched MAO double-barrier MTJs have shown enhanced quantum phenomena [83], an additional application of a temperature gradient to such a system might reveal interesting, new spin caloritronic effects.

Both barrier materials exhibited a doubling of the TMS ratio at a nominal barrier thickness of 2.6 nm from (4 to 8) % in case of MTJs with MAO barrier and from (12 to 25) % in case of MTJs with MgO barrier. Here, the RA products were in the same region of several $10^3\,\mathrm{k\Omega\mu m^2}$. MAO (MgO) based MTJs resulted in maximum TMS ratios of $8 \pm 1\,\%$ ($25 \pm 2\,\%$). This maximum is independent of the maximum TMR values of $32 \pm 1\,\%$ (MAO) and $151 \pm 7\,\%$ (MgO) located at nominal barrier thicknesses around 2 nm. As expected, since the TMS effect is dominated by the asymmetry of the DOS in contrast to the absolute number of states around μ in case of the TMR effect, a direct relation between the TMS and the TMR effect is not observed. The observed TMS peaks for thick barriers, which are independent of barrier material, are one of the main outcome of this work.

Up to now, theoretical as well as experimental studies have focused on barrier thicknesses of up to 2 nm and, therefore, are not able to explain the increasing TMS ratio of thick barriers. Further research is needed in order to understand the effects leading to the TMS peak. In particular, ab-initio calculations with respect to the differences of MAO and MgO as a barrier material are needed. They might also provide valuable

information on the thermal conductivities of thin tunneling barriers.

In addition to the enhanced TMS ratio, MAO based MTJs with a nominal barrier thickness of 2.6 nm reached very high thermovoltages of more than 350 μV. As a direct comparison, MgO based MTJs with the same nominal barrier thickness exhibited thermovoltages of around 100 μV in line with previous studies. The difference is explainable with regard to the thermal conductivities of both materials. Although there is an ongoing discussion about the thermal conductivity of thin insulating films and actual measurements are still lacking, MAO thin films are supposed to have a lower thermal conductivity than thin MgO films. Thus, the temperature difference across the MAO barrier is larger than the MgO barrier, which results in higher thermovoltages.

This finding is reinforced by the investigation of the remaining thermovoltages after a dielectric breakdown of the barrier. In case of MAO, the contribution of the intact barrier amounted to 70 % of the absolute thermovoltage of the intact MTJ, while it was 21 % for a comparable MgO MTJ. Hence, it was possible to calculate the thermal conductivities of the barriers with regard to the temperature differences occurring in the remaining stack, which are mostly due to the low thermal conductivity of the MnIr layer. The obtained value in case of MAO ($\approx 0.7\,\frac{\mathrm{W}}{\mathrm{Km}}$) corresponds very well to the theoretically suggested value and to the range of (0.3 to 2.3) $\frac{\mathrm{W}}{\mathrm{Km}}$ adopted in this work. In case of MgO, a value of 5.8 $\frac{\mathrm{W}}{\mathrm{Km}}$ was found with the same evaluation of the absolute thermovoltages after a dielectric breakdown. This value is close to the experimental value of 4 $\frac{\mathrm{W}}{\mathrm{Km}}$, found by Cahill et al. [89], but shows a discrepancy to the value of 0.9 $\frac{\mathrm{W}}{\mathrm{Km}}$ found by Kimling et al. [94] with a relatively new method based on MOKE experiments.

However, this evaluation relies on the simulated temperature differences within the MTJ and, consequently, can only be considered a rough estimate. More samples, for example with varying MnIr thickness and a vanishing barrier, might build a broader foundation for this technique. In the far future, MTJs with a specific layer structure might be used as Seebeck standards for nano-sized structures, since, in the meter-sized world, Seebeck coefficients are always measured in relation to a second material, which has a known Seebeck coefficient.

Nevertheless, COMSOL simulations of the thermal distributions within MTJs proved very useful during this work. In particular, they offered valuable insight into the huge temperature differences obtained with a focused laser beam in contrast to previous works. Additionally, the linear dependence of the temperature with increasing laser power was verified, which explains the linear dependence of the measured thermovoltage on the applied laser power. The simulated application of the laser beam to the contact pad instead of the MTJ resulted in a huge decrease of temperature difference across the barrier, which is also reflected by the decreased measured thermovoltage if the beam is moved away from the MTJ. However, the larger heating area of the contact pad results in an increased base temperature of the MTJ stack, which is also observed by increasing the size of the MTJ. It is unclear whether or not this effect is a parasitic contribution of the simulation. Nonetheless, the calculated Seebeck coefficients of MAO and MgO based MTJs are in good agreement with the results of preceding studies.

In addition to the problems tackled in this work, several other modules allow, for example, the implementation of time-dependence or Joule heating. However, the simulation of the thermal distribution of thin films does not differentiate between the interface thermal conductance and the electron-phonon thermal conductance, but rather assumes a uniform thermal conductivity of the whole thin film. The impact of this assumption is not yet clear. Nevertheless, the conjunction of remaining thermovoltage and COMSOL simulation lead to a new path regarding the thermal conductivity of thin insulating films, adding valuable content to the ongoing discussion.

Lastly, the direct comparison of the laser-induced and the intrinsic TMS revealed huge discrepancies. While the intrinsic results of the MgO MTJ differed by about three orders of magnitude, the results of the MAO based MTJs showed an opposite sign. Thus, a negative TMS effect was obtained, which directly contradicts the results of the laser-induced TMS. Additionally, very large TMS effects were artificially generated, which are not reproducible by the laser heating.

However, the Brinkman model offered an alternative way to explain the symmetries involved with the V/I data, which were previously used

to extract the Seebeck coefficients via the intrinsic method. Without any assumptions of Seebeck coefficients or temperature differences, the symmetries of simulated V/I Brinkman curves were able to cover all features. Furthermore, by changing the Brinkman barrier asymmetry, the symmetry of the V/I curve completely vanished or even changed its sign. Thus, the symmetry analysis is not suitable to explicitly identify any intrinsic TMS effect.

In addition, the Brinkman model proved to be very successful with regard to qualitative statements about samples with different barrier thicknesses. Although it is limited to systems without coherent tunneling and related band structure effects such as half-metallic ferromagnetism, the Brinkman model can significantly contribute to the knowledge about the barrier height and asymmetry as well as the actual barrier thickness. During this work, a comparison of the nominal with the Brinkman barrier thickness has been extremely valuable.

Another missing link within the TMS community is the direct comparison of the laser-induced and the extrinsic method. First attempts have been undertaken in cooperation with A. Boehnke, but failed so far due to the HL not being electrically isolated from the MTJ. Actual measurements are not too far away, since this is mostly a patterning problem. Additionally, experiments with a HL on top of the MTJ will be performed in a cryostat in Bielefeld, which will allow the deduction of the temperature dependence of the thermovoltage, the TMS ratio and the Seebeck coefficients.

All in all, this work provides a profound understanding of the arising thermovoltages and the accompanied TMS effect in laser-heated MTJs with different barrier materials and varying barrier thickness. It also states that the intrinsic TMS method results in Seebeck coefficients, which are not related to the results of actual laser-induced measurements. During all parts of this work, COMSOL simulations turned out to be a very useful addition when dealing with nano-sized structures and the occurring thermal distributions.

In conclusion, this work contributed a lot to the emerging and growing area of spin caloritronics. It advanced the research regarding thermal distributions inside MTJs and nano-sized structures. Moreover, this

work found that MAO is generally preferable when dealing with temperature differences in contrast to MgO. Thus, a new path to actual spin caloritronic applications is outlined.

Part V.

Appendices

A. Wentzel-Kramers-Brillouin approximation

Reference [29] assumes the following wave function

$$\Psi(x) = \exp\left(\frac{i}{\hbar}S(x)\right) \tag{9.1}$$

to solve the stationary one-dimensional Schrödinger equation

$$\frac{\mathrm{d}^2\Psi(x)}{\mathrm{d}x^2} + \frac{2m}{\hbar^2}(E - V(x))\Psi(x) = 0. \tag{9.2}$$

The solution is then given by

$$S'(x)^2 = 2m(E - V(x)) + i\hbar S''(x), \tag{9.3}$$

where $2m(e-V(x)) = p^2(x)$. Since the WKB approximation is a quasi-classical approximation terms with $\hbar$ are taken as correction factors and $\hbar \to 0$. Thus, $S(x)$ is Taylor expanded around $\hbar$

$$S(x) = S_0(x) + \frac{\hbar}{i}S_1(x) + ... \tag{9.4}$$

and with a combination of Eq. (9.3) and Eq. (9.4), the zeroth order term $S_0(x)$ is found, which directly leads to the first order term $S_1(x)$, if higher order terms are neglected. The complete first order solution is

$$S(x) \approx \pm \int p(x)\mathrm{d}x + \frac{\hbar}{i}\left[\ln\left(|S_0'(x)|^{-1/2}\right) + \mathrm{const}\right]. \tag{9.5}$$

This solution is inserted into Eq. (9.1) to get the wave function within the WKB approximation:

$$\Psi(x) \approx \frac{\text{const.}}{\sqrt{|p(x)|}} \exp\left(\pm \frac{i}{\hbar} \int p(x) \mathrm{d}x\right). \tag{9.6}$$

In order to use the first order term with $\hbar$ as correction factor, it has to be small in comparison to $p^2(x)$. Therefore, the WKB approximation is only valid if the change of the potential with the wavelength of the electron is much smaller than its kinetic energy ($\mathrm{d}V/\mathrm{d}x\lambda \ll E_{\mathrm{kin}}$). For a potential $V > E_{\mathrm{kin}}$, the transmission coefficient T becomes

$$T = \exp\left(-\frac{2}{\hbar} \int_0^d \sqrt{2m(V(x) - E)} \mathrm{d}x\right). \tag{9.7}$$

Reference [102] finds the WKB approximation to be applicable if the change in the potential from metal to insulator is not too sharp.

B. MATLAB interpolation procedure

In the following table the interpolation procedure to get V/I curves from measured I/V curves is described in chronological order.

MatLab Code	**Description**
data_I	current I measured at bias voltage V
data_V	applied bias voltage V
$\mathrm{step} = -\frac{(\min(\mathrm{data}_I) - \max(\mathrm{data}_I))}{\mathrm{length}(\mathrm{data}_I)}$	define step size between measured I values
$\mathrm{I}_- = 0 : \mathrm{step} : -\min(\mathrm{data}_I)$ $\mathrm{I}_+ = 0 : \mathrm{step} : \max(\mathrm{data}_I)$	define points with the distance of step size where the interpolation is performed
$\mathrm{interp}_+ = \mathrm{interp1q}(\mathrm{data}_I, \mathrm{data}_V, \mathrm{I}_+)$ $\mathrm{interp}_- = \mathrm{interp1q}(\mathrm{data}_I, \mathrm{data}_V, \mathrm{I}_-)$	result of interpolation, i.e., $V(I)$ for positive and negative branch
$\mathrm{V}_{\mathrm{asym}} = (\mathrm{interp}_{\mathrm{I}_-} - \mathrm{interp}_{\mathrm{I}_-})/2$ $\mathrm{V}_{\mathrm{sym}} = (\mathrm{interp}_{\mathrm{I}_+} + \mathrm{interp}_{\mathrm{I}_-})/2$ $\mathrm{I}_{\mathrm{asym}} = \mathrm{I}_+$ $\mathrm{I}^2_{\mathrm{sym}} = \mathrm{I}^2_+$	antisymmetric part as described in Sec. 3.4 symmetric part as described in Sec. 3.4 corresponding current I corresponding current squared I^2

C. Publications

T. Huebner, U. Martens, J. Walowski, A. Boehnke, J. Krieft, C. Heiliger, A. Thomas, G. Reiss, T. Kuschel, and M. Münzenberg. Enhancement of thermovoltage and tunnel magneto-Seebeck effect in CoFeB based magnetic tunnel junctions by variation of the $MgAl_2O_4$ and MgO barrier thickness. *Under review (2017).* `https://arxiv.org/abs/1706.08287`.

A. Boehnke, U. Martens, C. Sterwerf, A. Niesen, T. Huebner, M. von der Ehe, M. Meinert, T. Kuschel, A. Thomas, C. Heiliger. M. Münzenberg, and G. Reiss. Heusler compounds for spin caloritronics: Large magneto-Seebeck effects in magnetic tunnel junctions. *Under review (2017).* `https://arxiv.org/abs/1707.00505`.

U. Martens, J. Walowski, T. Schumann, M. Mansurova, A. Boehnke, T. Huebner, G. Reiss, A. Thomas, and M. Münzenberg. Pumping laser excited spins through MgO barriers. *J. Phys. D: Appl. Phys.*, 50:144003 (2017).

J. Kimling, G.-M. Choi, J.T. Brangham, T. Matalla-Wagner, T. Huebner, T. Kuschel, F. Yang, and D. G. Cahill. Picosecond Spin Seebeck Effect. *Phys. Rev. Lett.*, 118:057201 (2017).

T. Huebner, A. Boehnke, U. Martens, A. Thomas, J.-M. Schmalhorst, G. Reiss, M. Münzenberg, and T. Kuschel. Comparison of laser-induced and intrinsic tunnel magneto-Seebeck effect in CoFeB/$MgAl_2O_4$ and CoFeB/MgO magnetic tunnel junctions. *Phys. Rev. B*, 93:224433 (2016).

M. Meinert, T. Huebner, J. Schmalhorst, G. Reiss and E. Arenholz. Phase separation in Fe_2CrSi thin films. *J. Appl. Phys.*, 114:113908 (2013).

D. Conferences and colloquiums

03/2017 Talk at the 81st DPG spring meeting, Dresden, Germany

02/2017 Poster at Spinmechanics 4, Lake Louise, Canada

09/2016 Poster at SWI workshop, Greifswald, Germany

08/2016 Talk at PhD workshop, Mainz, Germany

07/2016 Poster at Spin caloritronics 7, Utrecht, Netherlands

03/2016 Talk at the 80th DPG spring meeting, Regensburg, Germany

03/2016 Poster at the Colloquium of the SPP 1538, Bad Honnef, Germany

03/2015 Poster at the 79th DPG spring meeting, Berlin, Germany

02/2015 Poster at the Colloquium of the SPP 1538, Bad Honnef, Germany

07/2014 Poster at the Spin caloritronics 6, Irsee, Germany

03/2014 Poster at the 78th DPG spring meeting, Dresden, Germany

Danksagung

An dieser Stelle bedanke ich mich für die fortwährende Unterstützung zahlreicher Menschen, ohne die diese Arbeit niemals gelungen wäre. Außerdem bin ich dankbar für die finanzielle Unterstützung der Deutschen Forschungsgemeinschaft (DFG) im Rahmen des Schwerpunktprogramms „Spin Caloric Transport“ (SPP 1538), der Wilhelm und Else Heraeus-Stiftung und der University of Alabama.

Günter Reiss danke ich für die Erstbegutachtung und die Möglichkeit meine Doktorarbeit in einem zukunftsträchtigen, interessanten und internationalen Bereich zu verfassen. Vielen Dank auch an Thomas Huser für die unkomplizierte Zweitbegutachtung. Ein ganz besonderer Dank gilt Timo Kuschel, der mit zahlreichen Diskussionen und Hilfestellungen maßgeblich zum erfolgreichen Verlauf meines Doktorandentums beigetragen hat.

Alexander Böhnke danke ich für die großartige Unterstützung im Labor und die Gelassenheit außerhalb. Ganz besonders werden mir die Fahrten nach Greifswald und der obligatorische Pflaumenaugust im Gedächtnis bleiben. In Greifswald haben viele Leute Anteil an den erfolgreichen Messungen, die die Basis dieser Doktorarbeit bilden. Besonders hervorzuheben sind dabei Ulrike Martens und Jakob Walowski, die meine Aufenthalte in Greifswald stets abwechslungsreich und lehrreich gestaltet haben. Natürlich darf auch Markus Münzenberg nicht fehlen, der sein Labor, seine Erfahrung und seine Zeit zur Verfügung gestellt hat. Dank Euch werde ich Greifswald immer als offene und schöne Stadt in Erinnerung behalten!

I would like to thank the MINT Center and the University of Alabama for creating the possibility to join their Internship Program. In addition, I would like to thank my supervisor Prof. Arunava Gupta, who always had time and good advice independent of topic or issue. Amit Vikram Singh

and Zhong Li made the lab work a unique, positive memory. Not only did they have new ideas and insights in times of encountering stumbling blocks, they also had a smile on their lips every day. Thank you guys. At last I would like to mention the hard working people behind the scenes. Jamie Crawford, Carrie Martin, Casey McDow, Jason Foster, Dr. Michael Buettner and of course Dr. Takao Suzuki made sure that everything went perfect, from luncheons, to field trips to lab trainings. My time in the US and at the University of Alabama was a very positive experience that I will not forget for the rest of my life.

Eine weitere fruchtbare Kooperation ist im Laufe dieser Arbeit mit Johannes Kimling entstanden, der einige Proben aus meiner Zeit in Alabama für seine Experimente nutzen konnte. Zusätzlich hat ein reger Probenaustausch und die Ermittlung von thermischen Leitfähigkeiten mittels MOKE-Experimenten die Diskussion meiner Ergebnisse vorangetrieben. Vielen Dank! Christian Heiliger danke ich für die theoretischen Berechnungen rund um den Tunnel Magneto-Seebeck Effekt und viele allgemeine Einblicke in die Welt des theoretischen Physikers.

In Bielefeld hat vor allem Jan Michael-Schmalhorst durch gezielte fachliche, aber auch persönliche Gespräche meine Arbeit in die richtigen Bahnen gelenkt. Außerdem danke ich den folgenden D2'lern für die unermüdliche Hilfe im Labor und die vielen schönen Momente abseits der Arbeit: Christian Sterwerf, Christoph Klewe, Lars Helmich, Luca Marnitz, Andreas „Manni“ Becker, Markus Meinert, Jan Balluf, Gerhard Götz, Marianne Bartke, Karsten Rott, Niklas Dohmeier, Philipp Zilske, Mareike Dunz, Norman Shepheard, Lauritz Schnatmann, Denis Dyck, Jan Krieft, Tristan Matalla-Wagner, Alessia Niesen, Daniel Meier, Orestis Manos, Panagiota Bougiatioti und Andy Thomas. Zusätzlich danke ich Aggi Windmann für die administrative Unterstützung.

Außerdem kann ich nicht sagen, was aus mir und meiner Arbeit ohne Oliver Reimer, Robin Klett und Matthias Simonis geworden wäre. Die täglichen (manchmal auch stündlichen) Kaffeepausen mit Euch haben die dunklen Seiten der Promotion erhellt und das gemeinsame Feiern von Erfolgen versüßt. Ich bin euch ewig dankbar! Außerhalb der Universität haben Thomas Lilienkamp, Hanno Meyer zu Theenhausen, Michael Stührenberg, Jan Haskenhoff, Benedikt „Annihilat0r“ Brink und Wilko

Lührs entscheidend dazu beigetragen meine Gedanken zu ordnen und den Fokus nicht zu verlieren. Vielen Dank zudem an Alexander Burgdorf, der meine Arbeit aufmerksam gelesen und korrigiert hat.

Meiner Mutter Annette danke ich von ganzem Herzen für den emotionalen Beistand und den bedingungslosen Rückhalt. Meinem Vater Hans-Joachim danke ich für die Hilfe bei der Findung und der Unterstützung bei der Beschreitung des richtigen Weges. Vielen Dank an meine restliche Familie für die Geduld und die schönen Momente abseits der Pflicht. Ohne Euch wäre ich niemals so weit gekommen.

Zuletzt danke ich meiner geliebten Frau Jenny, die mir jeden Tag aufs Neue hilft die wichtigen Dinge im Leben nicht aus den Augen zu verlieren. Dein Lachen, deine Energie und deine Liebe sind mein Glück und meine Hoffnung. Du vervollständigst mich. Danke, für immer.

VI. Bibliography

[1] G.E. Moore. Cramming more components onto integrated circuits. *IEEE Solid-State Circuits Mag.*, 38:114, 1965.

[2] ITRS 2.0. International Technology Roadmap for Semiconductors. `http://www.itrs2.net/`, 2015. [Online; accessed 25-July-2017].

[3] M. Mitchell Waldrop. More than Moore. *Nature*, 530:145, 2016.

[4] S. Ikeda, J. Hayakawa, Y. Ashizawa, Y.M. Lee, K. Miura, H. Hasegawa, M. Tsunoda, F. Matsukura, and H. Ohno. Tunnel magnetoresistance of 604 % at 300 K by suppression of Ta diffusion in CoFeB/MgO/CoFeB pseudo-spin-valves annealed at high temperature. *Appl. Phys. Lett.*, 93:082508, 2008.

[5] Ltd. MultiDimension Technology Co. MultiDimension - Sensing the Future. `http://www.dowaytech.com/en/sensor.html`, 2017. [Online; accessed 04-July-2017].

[6] Lawrence Livermore National Laboratory and the Department of Energy. Estimated U.S. energy consumption in 2016. `https://flowcharts.llnl.gov/content/assets/docs/2016_United-States_Energy.pdf`, 2016. [Online; accessed 19-May-2017].

[7] M. Johnson and R.H. Silsbee. Thermodynamic analysis of interfacial transport and of the thermomagnetoelectric system. *Phys. Rev. B*, 35:4959, 1987.

[8] K. Uchida, S. Takahashi, K. Harii, J. Ieda, W. Koshibae, K. Ando, S. Maekawa, and E. Saitoh. Observation of the spin Seebeck effect. *Nature*, 455:778, 2008.

[9] G.E.W. Bauer, A.H. Mac Donald, and S. Maekawa. Spin caloritronics. *Solid State Commun*, 150:459, 2010.

[10] G.E.W. Bauer, E. Saitoh, and B.J. van Wees. Spin caloritronics. *Nat. Mater.*, 11:391, 2012.

[11] M. Czerner, M. Bachmann, and C. Heiliger. Spin caloritronics in magnetic tunnel junctions: Ab initio studies. *Phys. Rev. B*, 83:132405, 2011.

[12] M. Walter, J. Walowski, V. Zbarsky, M. Münzenberg, M. Schäfers, D. Ebke, G. Reiss, A. Thomas, P. Peretzki, M. Seibt, J.S. Moodera, M. Czerner, M. Bachmann, and C. Heiliger. Seebeck effect in magnetic tunnel junctions. *Nat. Mater.*, 10:742, 2011.

[13] N. Liebing, S. Serrano-Guisan, K. Rott, G. Reiss, J. Langer, B. Ocker, and H.W. Schumacher. Tunneling Magnetothermopower in Magnetic Tunnel Junction Nanopillars. *Phys. Rev. Lett.*, 107:177201, 2011.

[14] A. Messiah. *Quantum Mechanics*. North-Holland, Amsterdam, 1962.

[15] M. Julliere. Tunneling between ferromagnetic films. *Phys. Lett.*, 54A:225, 1975.

[16] J.C. Slonczewski. Conductance and exchange coupling of two ferromagnets seperated by a tunneling barrier. *Phys. Rev. B*, 39:6995, 1989.

[17] J.S. Moodera, L.R. Kinder, T.M. Wong, and R. Meservey. Large Magnetoresistance at Room Temperature in Ferromagnetic Thin Film Tunnel Junctions. *Phys. Rev. Lett.*, 74:3273, 1995.

[18] T. Miyazaki and N. Tezuka. Giant magnetic tunneling effect in $Fe/Al_2O_3/Fe$ junction. *J. Magn. Magn. Mater.*, 139:231, 1995.

[19] J. Noguesa and I.K. Schullerb. Exchange bias. *J. Magn. Magn. Mater.*, 192:203, 1999.

[20] N.W. Ashcroft and N. Mermin. *Solide State Physics*. Cengage Learning, Inc, 1976.

[21] R. Meservey and P.M. Tedrow. Spin-polarized electron tunneling. *Phys. Rep.*, 238:173, 1994.

[22] S. Parkin, X. Jiang, C. Kaiser, A. Panchula, K. Roche, and M. Samant. Magnetically Engineered Spintronic Sensors and Memory. *Proc. IEEE*, 91:661, 2003.

[23] S. Yuasa, T. Nagahama, and Y. Suzuki. Spin-Polarized Resonant Tunneling in Magnetic Tunnel Junctions. *Science*, 297:234, 2002.

[24] T. Nagahama, S. Yuasa, E. Tamura, and Y. Suzuki. Spin-Dependent Tunneling in Magnetic Tunnel Junctions with a Layered Antiferromagnetic Cr(001) Spacer: Role of Band Structure and Interface Scattering. *Phys. Rev. Lett.*, 95:086602, 2005.

[25] W.H. Butler, Y.-G. Zhang, and T.C. Schulthess. Spin-dependent tunneling conductance of Fe|MgO|Fe sandwiches. *Phys. Rev. B*, 63:054416, 2001.

[26] S. Yuasa and D.D. Djayaprawira. Giant tunnel magnetoresistance in magnetic tunnel junctions with a crystalline MgO(001) barrier. *J. Phys. D: Appl. Phys.*, 40:R337, 2007.

[27] J.G. Simmons. Generalized Formula for the Electric Tunnel Effect between Similar Electrodes Separated by a Thin Insulating Film. *J. Appl. Phys.*, 34:1793, 1963.

[28] W.F. Brinkman, R.C. Dynes, and J.M. Rowell. Tunneling Conductance of Asymmetrical Barriers. *J. Appl. Phys.*, 41:1915, 1970.

[29] T. Fließbach. *Quantenmechanik*. Spektrum Akademischer Verlag, 2000.

[30] M. Meinert. The Heusler Alloy CoMnSb in Magnetic Tunnel Junctions and High Temperature TMR Measurements. Master's thesis, Bielefeld University, 2008.

[31] R. Gross and A. Marx. *Festkörperphysik*. Oldenbourg Wissenschaftsverlag, 2012.

[32] A. Boehnke. *Tunnel magneto-Seebeck effect: Improving the effect size*. PhD thesis, Bielefeld University, Department of Physics, 2016.

[33] Ioffe Institue. Silicon. `http://www.ioffe.ru/SVA/NSM/Semicond/Si/electric.html#Basicf`, 2001. [Online; accessed 29-June-2017].

[34] U. Sivan and Y. Imry. Multichannel Landauer formula for thermoelectric transport with application to thermopower near the mobility edge. *Phys. Rev. B*, 33:551, 1986.

[35] C. Heiliger, C. Franz, and M. Czerner. Ab initio studies of the tunneling magneto-Seebeck effect: Influence of magnetic material. *Phys. Rev. B*, 87:224412, 2013.

[36] M. Bachmann, M. Czerner, and C. Heiliger. Calculation of Thermoelectric Transport Properties in Heterostructures. *J. Electron. Mater.*, 40:577, 2011.

[37] B. Geisler and P. Kratzer. Spincaloric properties of epitaxial Co_2MnSi / MgO / Co_2MnSi magnetic tunnel junctions. *Phys. Rev. B*, 92:144418, 2015.

[38] D. Comtesse, B. Geisler, P. Entel, P. Kratzer, and L. Szunyogh. First-principles study of spin-dependent thermoelectric properties of half-metallic Heusler thin films between platinum leads. *Phys. Rev. B*, 89:094410, 2014.

[39] C.L.-Monis, A.M.-Abiague, and J. Fabian. Tunneling anisotropic thermopower and Seebeck effects in magnetic tunnel junctions. *Phys. Rev. B*, 90:174426, 2014.

[40] C.L.-Monis, A.M.-Abiague, and J. Fabian. Tunneling magnetothermopower in magnetic tunnel junctions. *Phys. Rev. B*, 89:054419, 2014.

[41] A. Boehnke, M. Walter, N. Roschewsky, T. Eggebrecht, V. Drewello, K. Rott, M. Münzenberg, A. Thomas, and G. Reiss. Time-resolved measurement of the tunnel magneto-Seebeck effect in a single magnetic tunnel junction. *Rev. Sci. Instrum.*, 84:063905, 2013.

[42] Y. Xu, W. Lin, S.P.-Watelot, M. Hehn, H. Rinnert, Y. Lu, F. Montaigne, D. Lacour, S. Andrieu, and S. Mangin. Origins of large light induced voltage in magnetic tunnel junctions grown on semiconductor substrates. *J. Appl. Phys.*, 119:023907, 2016.

[43] A. Boehnke, M. Milnikel, M. von der Ehe, C. Franz, V. Zbarsky, M. Czerner, K. Rott, A. Thomas, C. Heiliger, G. Reiss, and M. Münzenberg. On/off switching of bit readout in bias-enhanced tunnel magneto-Seebeck effect. *Sci. Rep.*, 5:8945, 2015.

[44] A. Boehnke, U. Martens, C. Sterwerf, A. Niesen, T. Huebner, M. von der Ehe, M. Meinert, T. Kuschel, A. Thomas, C. Heiliger, M. Münzenberg, and G. Reiss. Heusler compounds for spin caloritronics: Large magneto-Seebeck effects in magnetic tunnel junctions. `https://arxiv.org/abs/1707.00505`, 2017.

[45] N. Liebing, S. Serrano-Guisan, K. Rott, G. Reiss, J. Langer, B. Ocker, and H.W. Schumacher. Determination of spin-dependent Seebeck coefficients of CoFeB/MgO/CoFeB magnetic tunnel junction nanopillars. *J. Appl. Phys.*, 111:07C520, 2012.

[46] N. Liebing, S. Serrano-Guisan, P. Krzysteczko, K. Rott, G. Reiss, J. Langer, B. Ocker, and H.W. Schumacher. Tunneling magneto thermocurrent in CoFeB/MgO/CoFeB based magnetic tunnel junctions. *Appl. Phys. Lett.*, 102:242413, 2013.

[47] N. Liebing, S. Serrano-Guisan, K. Rott, G. Reiss, and H.W. Schumacher. Noise spectroscopy of CoFeB/MgO/CoFeB magnetic tunnel junctions in the presence of thermal gradients. *J. Magn. Magn. Mater.*, 400:154, 2016.

[48] T. Böhnert, S. Serrano-Guisan, E. Paz, B. Lacoste, R. Ferreira, and P.P. Freitas. Magnetic tunnel junctions with integrated thermometers for magnetothermopower measurements. *J. Phys.: Condens. Matter*, 29:185303, 2017.

[49] T. Böhnert, R. Dutra, R.L. Sommer, E. Paz, S. Serrano-Guisan, R. Ferreira, and P.P. Freitas. Influence of the thermal interface resistance on the thermovoltage of a magnetic tunnel junction. *Phys. Rev. B*, 95:104441, 2017.

[50] J. Shan, F.K. Dejene, J.C. Leutenantsmeyer, J. Flipse, M. Münzenberg, and B.J. van Wees. Comparison of the magneto-Peltier and magneto-Seebeck effects in magnetic tunnel junctions. *Phys. Rev. B*, 92:020414(R), 2015.

[51] J.-C. Le Breton, S. Sharma, H. Saito, S. Yuasa, and R. Jansen. Thermal spin current from a ferromagnet to silicon by Seebeck spin tunneling. *Nature*, 475:82, 2011.

[52] Z.H. Zhang, Y.S. Gui, L. Fu, X.L. Fan, J.W. Cao, D.S. Xue, P.P. Freitas, D. Houssameddine, S. Hemour, K. Wu, and C.-M. Hu. Seebeck Rectification Enabled by Intrinsic Thermoelectrical Coupling in Magnetic Tunnel Junctions. *Phys. Rev. Lett.*, 109:037206, 2012.

[53] J.M. Teixeira, J.D. Costa, J. Ventura, M.P. Fernandez-Garcia, J. Azevedo, J.P. Araujo, J.B. Sousa, P. Wisniowski, S. Cardoso, and P.P. Freitas. Giant intrinsic thermomagnetic effects in thin MgO magnetic tunnel junctions. *Appl. Phys. Lett.*, 102:212413, 2013.

[54] S.S.P. Parkin, C. Kaiser, A. Panchula, P.M. Rice, B. Hughes, M. Samant, and S.-H. Yang. Giant tunnelling magnetoresistance at room temperature with MgO (100) tunnel barriers. *Nat. Mater.*, 31:862, 2004.

[55] S. Yuasa, T. Nagahama, A. Fukushima, Y. Sizuki, and K. Ando. Giant room-temperature magnetoresistance in single-

crystal Fe/MgO/Fe magnetic tunnel junctions. *Nat. Mater.*, 3:868, 2004.

[56] D. Wang, C. Nordman, J.M. Daughton, Z. Qian, and J. Fink. 70 % TMR at Room Temperature for SDT Sandwich Junctions with CoFeB as Free and Referance Layers. *IEEE Trans. Magn.*, 40:2269, 2004.

[57] J. Mathon and A. Umerski. Theory of tunneling magnetoresistance of an epitaxial Fe/MgO/Fe(001) junction. *Phys. Rev. B*, 63:220403(R), 2001.

[58] W.H. Butler, X.-G. Zhang, T.C. Schulthess, and J.M. MacLaren. Spin-dependent tunneling conductance of Fe | MgO | Fe sandwiches. *Phys. Rev. B*, 63:054416, 2001.

[59] W.J. Gallagher, S.S.P. Parkin, Y. Lu, X.P. Bian, A. Marley, K.P. Roche, R.A. Altman, S.A. Rishton, C. Jahnes, T.M. Shaw, and G. Xiao. Microstructured magnetic tunnel junctions. *J. Appl. Phys.*, 81(3741), 1997.

[60] R.C. Sousa, J.J. Sun, V. Soares, P.P. Freitas, A. Kling, M.F. da Silva, and J.C. Soares. Large tunneling magnetoresistance enhancement by thermal anneal. *Appl. Phys. Lett.*, 73(3288), 1998.

[61] S.S.P. Parkin, K.P. Roche, M.G. Samant, P.M. Rice, R.B. Beyers, R.E. Scheuerlein, E.J. O'Sullivan, S.L. Brown, J. Bucchigano, D.W. Abraham, Y. Lu, M. Rooks, P.L. Trouilloud, R.A. Wanner, and W.J. Gallagher. Exchange-biased magnetic tunnel junctions and application to nonvolatile magnetic random access memory. *J. Appl. Phys.*, 85(5828), 1999.

[62] S. Cardosa, P.P. Freitas, C. de Jesus, P. Wei, and J.C. Soares. Spin-tunnel-junction thermal stability and interface interdiffusion above 300 °C. *Appl. Phys. Lett.*, 76(610), 2000.

[63] A. Thomas, H. Brückl, M.D. Sacher, J. Schmalhorst, and G. Reiss. Aluminium oxidation by a remote electron cyclotron resonance

plasma in magnetic tunnel junctions. *J. Vac. Sci. Technol. B*, 21(2120), 2003.

[64] H.X. Wei, Q.H. Qin, M. Ma, R. Sharif, and X.F. Han. 80 % tunneling magnetoresistance at room temperature for thin Al-O barrier magnetic tunnel junction with CoFeB as free and reference layers. *J. Appl. Phys.*, 101(09B501), 2007.

[65] M. Bowen, V. Cros, F. Petroff, A. Fert, C. Boubeta, J.L. Costa-Krämer, J.V. Anguita, A. Cebollada, F. Briones, J.M. de Teresa, L. Morellon, M.R. Ibarra, F. Güell, F. Peiro, and A. Cornet. Large magnetoresistance in Fe/MgO/FeCo(001) epitaxial tunnel junctions on GaAs(001). *Appl. Phys. Lett.*, 79(1655), 2001.

[66] J. Faure-Vincent, C. Tiusan, E. Jouguelet, F. Canet, M. Sajieddine, C. Bellouard, E. Popova, M. Hehn, F. Montaigne, and A. Schuhl. High tunnel magnetoresistance in epitaxial Fe/MgO/Fe tunnel junctions. *Appl. Phys. Lett.*, 82(4507), 2003.

[67] D.D. Djayaprawira, K. Tsunekawa, M. Nagai, H. Maehara, S. Yamagata, N. Watanabe, S. Yuasa, Y. Suzuki, and K. Ando. 230 % room-temperature magnetoresistance in CoFeB/MgO/CoFeB magnetic tunnel junctions. *Appl. Phys. Lett.*, 86(092502), 2005.

[68] S. Yuasa, Y. Suzuki, T. Katayama, and K. Ando. Characterization of growth and crystallization processes in CoFeB/MgO/CoFeB magnetic tunnel junction structure by reflective high-energy electron diffraction. *Appl. Phys. Lett.*, 87(242503), 2005.

[69] S. Yuasa, A. Fukushima, H. Kubota, Y. Suzuki, and K. Ando. Giant tunneling magnetoresistance up to 410 % at room temperature in fully epitaxial Co/MgO/Co magnetic tunnel junctions with bcc Co(001) electrodes . *Appl. Phys. Lett.*, 89(042505), 2006.

[70] Y.M. Lee, J. Hayakawa, S. Ikeda, F. Matsukura, and H. Ohno. Effect of electrode composition on the tunnel magnetoresistance of pseudo-spin-valve magnetic tunnel junction with a MgO tunnel barrier. *Appl. Phys. Lett.*, 90(212507), 2007.

[71] Oliver Schebaum. *Bestimmung der Spinpolarisation durch supraleitende Tunnelspektroskopie*. PhD thesis, Bielefeld University, 2011.

[72] F. Bonell, S. Andrieu, C. Tiusan, and F. Montaigne. Influence of misfit dislocations on the magnetoresistance of MgO-based epitaxial magnetic tunnel junctions. *Phys. Rev. B*, 82:092405, 2010.

[73] R.C. Whited, C. J. Flaten, and W.C. Walker. Exciton Thermoreflectance of MgO and CaO. *Solid State Commun.*, 13:1903, 1973.

[74] U. Müller. *Anorganische Strukturchemie*. Teubner Studienbücher Chemie, 1996.

[75] V. Drewello, M. Schäfers, O. Schebaum, A.A. Khan, J. Münchenberger, J. Schmalhorst, G. Reiss, and A. Thomas. Inelastic electron tunneling spectra of MgO-based magnetic tunnel junctions with different electrode designs. *Phys. Rev. B*, 79:174417, 2009.

[76] C. Sterwerf, M. Meinert, J.-M. Schmalhorst, and G. Reiss. High TMR Ratio in Co_2FeSi and Fe_2CoSi Based Magnetic Tunnel Junctions. *IEEE Trans. Magn.*, 49:4386, 2013.

[77] J. Zhang, X.-G. Zhang, and X.F. Han. Spinel oxides: Δ_1 spin-filter barrier for a class of magnetic tunnel junctions. *Appl. Phys. Lett.*, 100:222401, 2012.

[78] Y. Miura, S. Muramoto, K. Abe, and M. Shirai. First-principles study of tunneling magnetoresistance in $Fe/MgAl_2O_4/Fe(001)$ magnetic tunnel junctions. *Phys. Rev. B*, 86:024426, 2012.

[79] H. Sukegawa, Y. Miura, S. Muramoto, S. Mitani, T. Niizeki, T. Ohkubo, K. Abe, M. Shirai, K. Inomata, and K. Hono. Enhanced tunnel magnetoresistance in a spinel oxide barrier with carion-site disorder. *Phys. Rev. B*, 86:184401, 2012.

[80] H. Sukegawa, S. Mitani, T. Ohkubo, K. Inomata, and K. Hono. Low-resistive monocrystalline Mg-Al-O barrier magnetic tunnel junctions for spin-transfer magnetization switching. *Appl. Phys. Lett.*, 103:142409, 2013.

[81] M. Belmoubarik, H. Sukegawa, T. Ohkubo, S. Mitani, and K. Hono. $MgAl_2O_4(001)$ based magnetic tunnel junctions made by direct sputtering of a sintered spinel target. *Appl. Phys. Lett.*, 108:132404, 2016.

[82] T. Scheike, H. Sukegawa, K. Inomata, T. Ohkubo, K. Hono, and S. Mitani. Chemical ordering and large tunnel magnetoresistance in $Co_2FeAl/MgAl_2O_4/Co_2FeAl(001)$ junctions. *Appl. Phys Express*, 9:053004, 2016.

[83] B.S. Tao, H.X. Yang, Y.L. Zuo, X. Devaux, G. Lengaigne, M. Hehn, D. Lacour, S. Andrieu, M. Chshiev, T. Hauet, F. Montaigne, S. Mangin, X.F. Han, and Y. Lu. Long-Range Phase Coherence in Double-Barrier Magnetic Tunnel Junctions with a Large Thick Metallic Quantum Well. *Phys. Rev. Lett.*, 115:157204, 2015.

[84] T. Huebner. Phase separation in Fe_2CrSi thin films and Spinel based Magnetic Tunnel Junctions. Master's thesis, Universität Bielefeld, 2014.

[85] B. Tao, D. Li, H. Liu, H. Wei, J.-F. Feng, S. Wang, and X. Han. Transport Properties in Sputtered $CoFeB/MgAl_2O_4/CoFeB$ Magnetic Tunnel Junctions. *IEEE Trans. Magn.*, 50:4401004, 2014.

[86] A. Boehnke. Tunnel-Magneto-Seebeck-Effekt. Master's thesis, Universität Bielefeld, 2012.

[87] J.M. Khosrofian and B.A. Garetz. Measurement of a Gaussian laser beam diameter through the direct inversion of knife-edge data. *Appl. Opt.*, 22:3406, 1983.

[88] Y. Suzaki and A. Tachibana. Measurement of the μm sized radius of Gaussian laser beam using the scanning knife-edge. *Appl. Opt.*, 14:2809, 1975.

[89] S.-M. Lee, D.G. Cahill, and T.H. Allen. Thermal conductivity of sputtered oxide films. *Phys. Rev. B*, 52:253, 1995.

[90] G.A. Slack. Thermal Conductivity of MgO, Al_2O_3, $MgAl_2O_4$, and Fe_3O_4 Crystals from 3° to 300 °K. *Phys. Rev.*, 126:427, 1962.

[91] St. Burghartz and B. Schulz. Thermophysical properties of sapphire, AlN and $MgAl_2O_4$ down to 70 K. *J. Nucl. Mater.*, 212-215:1065, 1994.

[92] S. Klemme and M. Ahrens. Low-temperature heat capacities of $MgAl_2O_4$ and spinels of the $MgCr_2O_4$-$MgAl_2O_4$ solid solution. *Phys. Chem. Miner.*, 34:59, 2007.

[93] J. Zhang, M. Bachmann, M. Czerner, and C. Heiliger. Thermal transport and non-equlibrium temperature drop across a magnetic nanostructured interface. *Phys. Rev. Lett.*, 115:037203, 2015.

[94] J. Kimling and D.G. Cahill. Thermische Leitfähigkeit dünner MgO Schichten. Private communication.

[95] Z.L. Wu, M. Reichling, X.-Q. Hu, K. Balasubramanian, and K.H. Guenther. Absorption and thermal conductivity of oxide thin films measured by photothermal displacement and reflectance methods. *Appl. Opt.*, 32:5660, 1993.

[96] K.T. Jacob, C. Shekhar, and Y. Waseda. An update on the thermodynamics of Ta_2O_5. *J. Chem. Thermodyn.*, 41:748, 2009.

[97] C. Papusoi, R. Sousa, J. Herault, I.L. Prejbeanu, and B. Dieny. Probing fast heating in magnetic tunnel junction structures with exchange bias. *New J. Phys.*, 10:103006, 2008.

[98] J. Zhang, X.G. Zhang, and X.F. Han. Spinel oxides: Δ_1 spin-filter barrier for a class of magnetic tunnel junctions. *Appl. Phys. Lett.*, 100:222401, 2012.

[99] U. Martens, J. Walowski, T. Schumann, M. Mansurova, A. Boehnke, T. Huebner, G. Reiss, A. Thomas, and M. Münzenberg. Pumping laser excited spins through MgO barriers. *J. Phys. D: Appl. Phys.*, 50:144003, 2017.

[100] P. Krzysteczko, X. Hu, N. Liebing, S. Sievers, and H.W. Schumacher. Domain wall magneto-Seebeck effect. *Phys. Rev. B*, 92:140405(R), 2015.

[101] T. Huebner, A. Boehnke, U. Martens, A. Thomas, J.-M. Schmalhorst, G. Reiss, M. Münzenberg, and T. Kuschel. Comparison of laser-induced and intrinsic tunnel magneto-Seebeck effect in CoFeB/$MgAl_2O_4$ and CoFeB/MgO magnetic tunnel junctions. *Phys. Rev. B*, 93:224433, 2016.

[102] W.A. Harrison. Tunneling from an Independent-Particle Point of View. *Phys. Rev.*, 123:85, 1961.